

**Victor A. Maltsev and Edward G. Lakatta**

*Am J Physiol Heart Circ Physiol* 296:594-615, 2009. First published Jan 9, 2009;  
doi:10.1152/ajpheart.01118.2008

**You might find this additional information useful...**

---

Supplemental material for this article can be found at:

<http://ajpheart.physiology.org/cgi/content/full/01118.2008/DC1>

This article cites 69 articles, 42 of which you can access free at:

<http://ajpheart.physiology.org/cgi/content/full/296/3/H594#BIBL>

This article has been cited by 1 other HighWire hosted article:

**Beating to time: calcium clocks, voltage clocks, and cardiac pacemaker activity**

D. A. Eisner and E. Cerbai

*Am J Physiol Heart Circ Physiol*, March 1, 2009; 296 (3): H561-H562.

[Full Text] [PDF]

Updated information and services including high-resolution figures, can be found at:

<http://ajpheart.physiology.org/cgi/content/full/296/3/H594>

Additional material and information about *AJP - Heart and Circulatory Physiology* can be found at:

<http://www.the-aps.org/publications/ajpheart>

---

This information is current as of June 1, 2009 .

## Synergism of coupled subsarcolemmal $\text{Ca}^{2+}$ clocks and sarcolemmal voltage clocks confers robust and flexible pacemaker function in a novel pacemaker cell model

Victor A. Maltsev and Edward G. Lakatta

Laboratory of Cardiovascular Science, Gerontology Research Center, National Institute on Aging, National Institutes of Health, Baltimore, Maryland

Submitted 24 October 2008; accepted in final form 4 January 2009

**Maltsev VA, Lakatta EG.** Synergism of coupled subsarcolemmal  $\text{Ca}^{2+}$  clocks and sarcolemmal voltage clocks confers robust and flexible pacemaker function in a novel pacemaker cell model. *Am J Physiol Heart Circ Physiol* 296: H594–H615, 2009. First published January 9, 2009; doi:10.1152/ajpheart.01118.2008.—Recent experimental studies have demonstrated that sinoatrial node cells (SANC) generate spontaneous, rhythmic, local subsarcolemmal  $\text{Ca}^{2+}$  releases ( $\text{Ca}^{2+}$  clock), which occur during late diastolic depolarization (DD) and interact with the classic sarcolemmal voltage oscillator (membrane clock) by activating  $\text{Na}^+$ - $\text{Ca}^{2+}$  exchanger current ( $I_{\text{NCX}}$ ). This and other interactions between clocks, however, are not captured by existing essentially membrane-delimited cardiac pacemaker cell numerical models. Using wide-scale parametric analysis of classic formulations of membrane clock and  $\text{Ca}^{2+}$  cycling, we have constructed and initially explored a prototype rabbit SANC model featuring both clocks. Our coupled oscillator system exhibits greater robustness and flexibility than membrane clock operating alone. Rhythmic spontaneous  $\text{Ca}^{2+}$  releases of sarcoplasmic reticulum (SR)-based  $\text{Ca}^{2+}$  clock ignite rhythmic action potentials via late DD  $I_{\text{NCX}}$  over much broader ranges of membrane clock parameters [e.g., L-type  $\text{Ca}^{2+}$  current ( $I_{\text{CaL}}$ ) and/or hyperpolarization-activated (“funny”) current ( $I_f$ ) conductances]. The system  $\text{Ca}^{2+}$  clock includes SR and sarcolemmal  $\text{Ca}^{2+}$  fluxes, which optimize cell  $\text{Ca}^{2+}$  balance to increase amplitudes of both SR  $\text{Ca}^{2+}$  release and late DD  $I_{\text{NCX}}$  as SR  $\text{Ca}^{2+}$  pumping rate increases, resulting in a broad pacemaker rate modulation (1.8–4.6 Hz). In contrast, the rate modulation range via membrane clock parameters is substantially smaller when  $\text{Ca}^{2+}$  clock is unchanged or lacking. When  $\text{Ca}^{2+}$  clock is disabled, the system parametric space for fail-safe SANC operation considerably shrinks: without rhythmic late DD  $I_{\text{NCX}}$  ignition signals membrane clock substantially slows, becomes dysrhythmic, or halts. In conclusion, the  $\text{Ca}^{2+}$  clock is a new critical dimension in SANC function. A synergism of the coupled function of  $\text{Ca}^{2+}$  and membrane clocks confers fail-safe SANC operation at greatly varying rates.

calcium; sarcoplasmic reticulum; ion channels; numerical modeling; sinoatrial node cell

NUMERICAL MODELS SIMULATING dynamic interplay of multiple processes have been invaluable assets for the achievement of mechanistic insights into the complex function of excitable cells, including cardiac cells. Landmark quantitative models describing how membrane ion channels interact as a function of time and voltage underlie the quantitative theory of membrane excitation by Hodgkin and Huxley, which, in 1960, was modified to simulate spontaneous action potentials (APs) of

cardiac pacemaker cells (46). Subsequently, a large cohort of essentially membrane-delimited models of sinoatrial nodal cells (SANC, the primary pacemakers of the heart) evolved with each newer model [12 models since 1980 (71)] specifying novel ion current properties commensurate with their discovery in voltage-clamp studies.

However, since seminal studies by Bozler (6) in 1943, substantial experimental evidence indicates that all cardiac cells, including pacemaker cells, possess another oscillator of subcellular origin that can work independently of sarcolemma (reviewed in Ref. 43). In 1979, summarizing results on oscillatory membrane currents under voltage clamp in cardiac Purkinje cells, Tsien et al. (63) suggested a new concept of cardiac pacemaker oscillations based on interactions of “a surface membrane oscillator” and “an internal oscillator” with “cycles of  $\text{Ca}^{2+}$  uptake and release by the sarcoplasmic reticulum” (SR). However, this concept was abandoned because recording the oscillatory  $\text{Ca}^{2+}$  signals by techniques of that time required conditions of strong  $\text{Ca}^{2+}$  signal amplification associated with  $\text{Ca}^{2+}$  overload and pathological function. Accordingly, the internal  $\text{Ca}^{2+}$  oscillator of some existing cardiac cell numerical models initiates abnormal cardiac impulses under the conditions of  $\text{Na}^+$  and  $\text{Ca}^{2+}$  overload (47).

The concept that interacting oscillators drive normal cardiac automaticity has recently emerged as further data, obtained with more precise experimental techniques, have demonstrated a substantial contribution of  $\text{Ca}^{2+}$  cycling by SR to the late phase of the diastolic depolarization (DD) of cardiac pacemaker cells under normal physiological conditions (reviewed in Ref. 41). Specifically, confocal imaging detects not only a global intracellular  $\text{Ca}^{2+}$  transient triggered by the AP, but also local, spontaneous  $\text{Ca}^{2+}$  releases (LCRs) from SR, which emerge beneath the cell membrane as multiple, relatively synchronous, locally propagating  $\text{Ca}^{2+}$  wavelets later in the cycle, i.e., during the late part of the DD (5, 21). LCRs activate the electrogenic operation of sarcolemmal  $\text{Na}^+$ - $\text{Ca}^{2+}$  exchanger (NCX), generating an inward current ( $I_{\text{NCX}}$ ) that imparts a steep, exponentially rising phase to the DD (4, 5, 21, 42). Importantly, SR indeed behaves as a true intracellular  $\text{Ca}^{2+}$  oscillator (Fig. 1), generating spontaneous rhythmic LCRs observed in voltage-clamped and chemically skinned SANC (70). Under voltage clamp, the  $\text{Ca}^{2+}$  oscillator generates oscillatory membrane current spikes of 10-pA scale (70) that are sufficient to drive critical late DD acceleration [see details in recent review (32)].

Address for reprint requests and other correspondence: E. G. Lakatta, Laboratory of Cardiovascular Science, Gerontology Research Center, NIA, NIH, 5600 Nathan Shock Dr., Baltimore, MD 21224-6825 (e-mail: LakattaE@grc.nia.nih.gov).

The costs of publication of this article were defrayed in part by the payment of page charges. The article must therefore be hereby marked “advertisement” in accordance with 18 U.S.C. Section 1734 solely to indicate this fact.

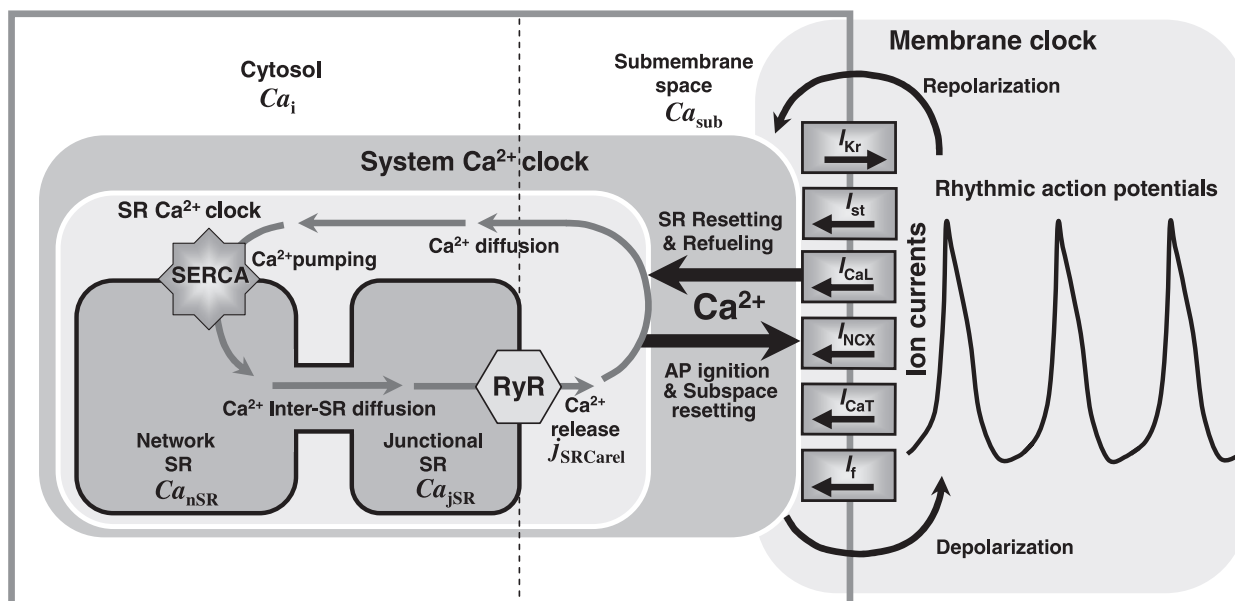


Fig. 1. Interacting  $\text{Ca}^{2+}$  clock and membrane clock in our model of rabbit sinoatrial node cells (SANC): schematic illustration of the cell compartments, major functional components, and their interactions approximated by our model. The physiological (full system)  $\text{Ca}^{2+}$  clock includes both the sarcoplasmic reticulum (SR)  $\text{Ca}^{2+}$  clock and balanced sarcolemmal  $\text{Ca}^{2+}$  fluxes of L-type  $\text{Ca}^{2+}$  current ( $I_{\text{CaL}}$ ) and  $\text{Na}^{+}$ - $\text{Ca}^{2+}$  exchanger (NCX) (bold arrows); see text for details.  $\text{Ca}_i$ ,  $\text{Ca}^{2+}$  in bulk cytosol;  $\text{Ca}_{\text{sub}}$ ,  $\text{Ca}^{2+}$  in the subspace; SERCA, SR  $\text{Ca}^{2+}$  pump;  $\text{Ca}_{\text{nSR}}$ ,  $\text{Ca}^{2+}$  in the network SR (nSR);  $\text{Ca}_{\text{jSR}}$ , junctional SR (jSR);  $j_{\text{SRCaRel}}$ , SR  $\text{Ca}^{2+}$  release rate global variable; RyR, cardiac ryanodine receptor; AP, action potential;  $I_{\text{Kr}}$ , rapid delayed rectifier current;  $I_{\text{st}}$ , sustained current;  $I_{\text{NCX}}$ , NCX current;  $I_{\text{CaT}}$ , T-type  $\text{Ca}^{2+}$  current;  $I_{\text{f}}$ , hyperpolarization-activated or “funny” current.

Under normal conditions,  $\text{Ca}^{2+}$  oscillations in SANC are driven not by  $\text{Ca}^{2+}$  overload but by the enhanced functional status of the  $\text{Ca}^{2+}$  cycling proteins due to relatively high levels (compared with ventricular myocytes) of both cAMP-dependent PKA (67) and CaMK II (CaMKII; Ref. 69) signaling in the basal state of SANC. Variability of the SR oscillator is achieved via gradations in the PKA signaling (67) and represents a novel major mechanism contributing to the pacemaker rate regulation via both  $\beta$ -adrenergic receptors ( $\beta$ -ARs; rate increase; Refs. 4, 65, 67) and muscarinic acetylcholine receptors (m-AChRs; rate decrease; Ref. 38).

Whereas these recent experimental results clearly suggest a new fundamental paradigm of cardiac pacemaker function, the integration of the membrane voltage oscillator and SR  $\text{Ca}^{2+}$  oscillator in normal SANC function has not been tested within a dynamic numerical cell model. Existing theoretical SANC models [recently reviewed by Wilders (71)] lack terms for late diastolic LCRs in submembrane space and do not capture the significance of the coupling of LCRs with sarcolemmal ion channels in initiation and regulation of normal basal SANC automaticity. Here, we present a prototype SANC model of dynamically interacting physiological  $\text{Ca}^{2+}$  oscillator and the classic membrane voltage oscillator (Fig. 1), recently dubbed “ $\text{Ca}^{2+}$  clock” and “membrane clock,” respectively (recent reviews in Refs. 32, 41). The model predicts spontaneous diastolic SR  $\text{Ca}^{2+}$  release in submembrane space and NCX current resulting in late DD acceleration. The model simulations not only validate the plethora of recent experimental findings, but also have discovered that it is the coupled function of  $\text{Ca}^{2+}$  clock and membrane clock that confers robustness and flexibility to cardiac pacemaker function.

## METHODS

### *Specific Aim of the Study and our Strategy to Develop and Explore the New Model*

The specific aim of our study was to develop a new numerical SANC model featuring interactions of  $\text{Ca}^{2+}$  and membrane clocks to explore novel mechanistic insights of cardiac impulse initiation. Our new SANC model is based on only a single new assumption: the existence of SR-based  $\text{Ca}^{2+}$  clock that was proven experimentally. Thus a major new feature of our SANC model is a more advanced and tuned formulation of the SR function. In the present study, we applied a wide-scale parameter sensitivity analysis of the dynamic system behavior (28, 64). Since performing analysis for all or many model parameters is nonrealistic (at least in 1 study), we have kept many parameters at their original classic values but varied only those few that are 1) reportedly different in SANC vs. ventricular myocytes, and 2) likely enhanced by a relatively high level of basal of cAMP/PKA-dependent signaling as discovered experimentally (67).

### *Approximation of SR $\text{Ca}^{2+}$ Release*

Our model adopts the formulation of cardiac ryanodine receptor (RyR) function developed by Shannon et al. (Ref. 59; referred throughout the paper as Shannon model) based on numerous experimental data on SR  $\text{Ca}^{2+}$  cycling in rabbit cardiomyocytes and an RyR gating scheme previously suggested by Stern et al. (60). The new advanced RyR formulations feature 1) Markov chain processes describing RyR activation and restitution kinetics, and 2) luminal  $\text{Ca}^{2+}$  regulation. Since the cardiac type RyR2 is the common major  $\text{Ca}^{2+}$  release channel type in SANC and ventricular myocytes, Shannon model served as a reasonable starting point in our quest, which approximates SR  $\text{Ca}^{2+}$  release rate by one global variable,  $j_{\text{SRCaRel}}$ . This rather simple approach was inspired by the experimental observations that individual multiple LCRs observed in SANC, in fact, become synchronized in SANC within 15–20% of the spontaneous cycle before subsequent membrane excitation (42, 70). Thus the

integrated LCR signal mass provides a strong whole cell signal that can be described by a global variable, such as  $j_{\text{SRCare1}}$ . In other words, the signals of individual LCRs emerging during late DD in submembrane space are integrated by  $\text{Ca}^{2+}$  sensing sarcolemmal proteins (such as NCX) and thus can be lumped (by frequency, size, duration, and amplitude) as a single  $\text{Ca}^{2+}$  release signal of the SR. We have validated this approach numerically in our prior, rather naïve SANC model (42) by describing phenomenologically (approximated with a sinusoidal function) this diastolic  $j_{\text{SRCare1}}$  signal of the synchronized LCRs: grading the timing and amplitude of this  $\text{Ca}^{2+}$  release signal (according to experimental data) indeed modulated the AP firing rate within the entire physiological range for rabbit SANC.

#### *Approximation of SR $\text{Ca}^{2+}$ Pump, Cell Structure, and $\text{Ca}^{2+}$ Buffering*

We have kept formulations of Kurata et al. (27) model of primary rabbit SANC (referred throughout the paper as Kurata model) for the SR  $\text{Ca}^{2+}$  pump, which were originally developed by Luo and Rudy (36), and for ion buffering in all cell compartments, including  $\text{Ca}^{2+}$  buffering by calsequestrin in junctional SR (jSR). We have also retained the original cell structure of the Kurata model consisting of four compartments: submembrane space (subspace), cytosol, network SR (nSR), and jSR (Fig. 1).

#### *Sarcolemmal Function*

Our model of sarcolemmal function also adopts formulations of Kurata model. We chose this particular model because it has, in our opinion, the most advanced and updated numerical formulations of the membrane function specific to rabbit primary SANC. Our basal state firing model has ion current parameters (listed in the data supplement online at the *AJP-Heart and Circulatory Physiology* web site) similar to those of our previously published modification of Kurata model (42). We have used this modified membrane model in other previous studies (4, 42, 67, 70) and have demonstrated that it describes rabbit SANC function more accurately than the original Kurata model. Specifically, it better describes the absolute values of systolic and diastolic intracellular  $\text{Ca}^{2+}$  that we measured in rabbit SANC (42). Also, compared with the original Kurata model, our modified model is very sensitive to SR  $\text{Ca}^{2+}$  releases (42, 70) [including individual stochastic LCRs (4, 67)], recapitulating numerous recent experimental results that demonstrate the critical importance of LCRs in SANC function and regulation [see recent reviews (32, 41, 45)]. Specifically, the original Kurata model has a relatively high L-type  $\text{Ca}^{2+}$  current ( $I_{\text{CaL}}$ ) conductance ( $g_{\text{CaL}}$ ) of 0.58 nS/pF vs. 0.385 and 0.29 nS/pF in Demir et al. (10) and Zhang et al. (73) models, respectively. Thus one of our important model modifications of the Kurata model was to reduce  $g_{\text{CaL}}$  by 20% (to 0.464 nS/pF). The problem with experimentally reported  $I_{\text{CaL}}$  densities, however, is their large spread. Furthermore,  $I_{\text{CaL}}$  density varies substantially from cell to cell even within each study. For example,  $I_{\text{CaL}}$  density varied from 3.8 to 11.4 pA/pF ( $7.7 \pm 2.3$  pA/pF, mean  $\pm$  SD) independently of cell size in a comprehensive study by Honjo et al. (17) of many rabbit SANC at 35°C and 0 mV (see Fig. 7B in Ref. 17). Our basal model simulates  $I_{\text{CaL}}$  of 6.9 pA/pF under these conditions, a value that is very close to their average. When  $\text{Ca}^{2+}$  clock is experimentally disabled by ryanodine (30  $\mu\text{M}$ ), the automaticity fails in majority of SANC [in 83% of cells (37)]. When we developed the model, the 20% decrease of  $g_{\text{CaL}}$  was required to reproduce this critical experimental result.

The importance of this and other changes to reproduce robust experimental results (e.g., with ryanodine) will be also clearly demonstrated in our wide-scale parametric system analysis (cf., RESULTS). We also compared AP characteristics and late DD ion currents of our basal firing model with those in prior SANC models and/or experimental data.

#### *Model Equations, Parameters, Variables, and Initial Conditions*

Our model is a system of 29 first-order differential equations. All model equations and parameter values are provided in the online data supplement. Table 1 lists all model variables ( $y_1$ – $y_{29}$ ) and their initial values. To avoid a lengthy transitional process in our parametric analysis, we set initial conditions for membrane clock gating variables ( $y_{15}$ – $y_{29}$ ) to "ready-to-fire" status, as if the sarcolemma was restituted at a low voltage (Table 1). Initial conditions for SR  $\text{Ca}^{2+}$  clock ( $y_1$ – $y_{14}$ ) were found as a set of instantaneous values of all variables for a mid-range  $\text{Ca}^{2+}$  oscillator (Fig. 3C), which will be described in RESULTS. The initial value for  $\text{Ca}^{2+}$  in the nSR ( $\text{Ca}_{\text{nSR}}$ ,  $y_4$ ) is 1.35 mM, which is within the physiological range of rabbit cardiac SR from 1 to 1.5 mM (58).

#### *Numerical Integration*

Source code for the model was developed using Borland Delphi 7 software. The model integration was performed with a fixed time step of 0.01 ms using a Pentium 4 (2.8 GHz)-based PC. Decreasing the integration step to 0.001 ms did not change results of simulations but substantially increased computation time.

#### *Finding Steady-State Solutions*

Since our model considers dynamic variations of voltage and ion concentrations, it belongs to so-called "second-generation" models (71). Whereas models of this type describe complex and physiologically realistic interplay of electrophysiological and ionic mechanisms, some models have problems with 1) "degeneracy," i.e., the existence of a continuum of equilibrium points, and 2) slow ion concentration drifts (Refs. 20, 24, 26 and reviewed in Ref. 71). For example, ion steady-state balance is achieved within hours of simulations in a model of atrial cell AP by Kneller et al. (24). A slow drift in Luo-Rudy dynamic model of ventricular cell was found to be due to the external stimulation current (20). Since our model does not apply external currents, a practical solution to the problems of drift and degeneracy was previously suggested to set the intracellular  $\text{Na}^+$  and  $\text{K}^+$  to constant values and treat them as independent model parameters (13, 71). Thus, as previously suggested by Kurata et al. (28), we fixed intracellular  $\text{Na}^+$  and  $\text{K}^+$  to 10 and 140 mM, respectively. Our parametric analysis of the system behavior was performed by a computer algorithm (online with simulations) that distinguished three types of steady-states: 1) steady rhythmic oscillations; 2) no oscillations or damped oscillations; and 3) chaotic oscillations. Steady oscillations were identified by the algorithm suggested previously by Kurata et al. (28): numerical integration was continued until the relative differences in both amplitude and period between the newly calculated cycle and the preceding cycle became  $<0.0005$  [2-dimensional (2-D) analysis] or  $<0.0001$  (1-dimensional analysis).

#### *Comparisons with Prior Models*

We compared some of our model predictions to those of previously published SANC models. For this comparison, we used traces from either a recently published review by Wilders (71) or from our own simulations using Cellular Open Resource (COR) developed and maintained by Alan Garny at Oxford University (<http://cor.physiol.ox.ac.uk>). COR can run numerous cell models, including classic SANC models, in CellML format available at <http://www.cellml.org>.

#### *Terminology*

*Spontaneous  $\text{Ca}^{2+}$  release.* Since our rather simple model of integrated  $\text{Ca}^{2+}$  dynamics does not describe stochastic, locally propagating  $\text{Ca}^{2+}$  releases within the subsarcolemmal space, we use the term "spontaneous release" here to describe the model SR  $\text{Ca}^{2+}$  release (variable  $j_{\text{SRCare1}}$ ), which is not induced by  $\text{Ca}^{2+}$  influx via

Table 1. Model variables: description and initial values

Variable	Initial Value	Description	
<i>SR Ca<sup>2+</sup> Clock</i>			
$y_1$	$Ca_i$	0.0001	Ca <sup>2+</sup> in myoplasm, mM
$y_2$	$Ca_{sub}$	0.000223	Ca <sup>2+</sup> in submembrane space, mM
$y_3$	$Ca_{jSR}$	0.029	Ca <sup>2+</sup> in the junctional SR (jSR), mM
$y_4$	$Ca_{nSR}$	1.35	Ca <sup>2+</sup> in the network SR (nSR), mM
$y_5$	$f_{TC}$	0.02	Fractional occupancy of the troponin Ca <sup>2+</sup> site by Ca <sup>2+</sup> in myoplasm
$y_6$	$f_{TMC}$	0.22	Fractional occupancy of the troponin Mg <sup>2+</sup> site by Ca <sup>2+</sup> in myoplasm
$y_7$	$f_{TMM}$	0.69	Fractional occupancy of the troponin Mg <sup>2+</sup> site by Mg <sup>2+</sup> in myoplasm
$y_8$	$f_{CMi}$	0.042	Fractional occupancy of calmodulin by Ca <sup>2+</sup> in myoplasm
$y_9$	$f_{CMs}$	0.089	Fractional occupancy of calmodulin by Ca <sup>2+</sup> in submembrane space
$y_{10}$	$f_{CQ}$	0.032	Fractional occupancy of calsequestrin by Ca <sup>2+</sup> in junctional SR
$y_{11}$	$R$	0.7499955	RyR reactivated (closed) state
$y_{12}$	$O$	$3.4 \times 10^{-6}$	RyR open state
$y_{13}$	$I$	$1.1 \times 10^{-6}$	RyR inactivated state
$y_{14}$	$RI$	0.25	RyR RI state (described in Refs. 59 and 60)
<i>Membrane Clock</i>			
$y_{15}$	$V_m$	-65	Membrane potential, mV
$y_{16}$	$d_L$	0	$I_{CaL}$ activation
$y_{17}$	$f_L$	1	$I_{CaL}$ voltage-dependent inactivation
$y_{18}$	$f_{Ca}$	1	$I_{CaL}$ Ca <sup>2+</sup> -dependent inactivation
$y_{19}$	$p_{aF}$	0	$I_{Kr}$ fast activation
$y_{20}$	$p_{aS}$	0	$I_{Kr}$ slow activation
$y_{21}$	$p_i$	1	$I_{Kr}$ inactivation
$y_{22}$	$n$	0	$I_{Ks}$ activation
$y_{23}$	$y$	1	$I_f$ activation
$y_{24}$	$d_T$	0	$I_{CaT}$ activation
$y_{25}$	$f_T$	1	$I_{CaT}$ inactivation
$y_{26}$	$q$	1	$I_{to}$ inactivation
$y_{27}$	$r$	0	$I_{to}$ and $I_{sus}$ activation
$y_{28}$	$q_a$	0	$I_{st}$ activation
$y_{29}$	$q_i$	1	$I_{st}$ inactivation

Our sinoatrial node cells (SANC) model is described by a system of 29 first-order differential equations given in the online data supplement (variables  $y_1 - y_{29}$ ). RyR, ryanodine receptor;  $I_{CaL}$ , L-type Ca<sup>2+</sup> current;  $I_{Kr}$ , rapid delayed rectifier current;  $I_{st}$ , sustained current;  $I_{CaT}$ , T-type Ca<sup>2+</sup> current;  $I_f$ , hyperpolarization-activated or "funny" current;  $I_{to}$ , transient outward current;  $I_{sus}$ , sustained component of the 4-AP-sensitive current.

$I_{CaL}$  during APs, but rather initiated by SR itself (e.g., during DD or when all membrane currents are set to 0).

**System robustness.** We determine robustness as the ability of the pacemaker cell system to perform, i.e., to generate normal, high-amplitude APs, when one or more key parameters of the system change. The larger the parameter variation without compromising the system performance, the more robust is the system.

## RESULTS

### SANC SR is a Release-Pumping-Delay Oscillator

It has been experimentally documented in chemically skinned and voltage-clamped SANC, in which effects of voltage-activated sarcolemmal ion currents are excluded, that the isolated SR is capable to spontaneously and rhythmically release Ca<sup>2+</sup> (67, 70). Thus our numerical SR subsystem (for variables  $y_1 - y_{14}$ , "SR Ca<sup>2+</sup> Clock" in Table 1) of the entire SANC model was first explored in isolation of membrane clock (all ion currents = 0) and tuned to operate as a self-sustained intracellular Ca<sup>2+</sup> oscillator in line with experimental results.

SR system behavior was numerically analyzed by grading two key parameters: SR Ca<sup>2+</sup> uptake rate ( $P_{up}$ ) and SR Ca<sup>2+</sup> release rate constant ( $k_s$ ). We chose these parameters because: 1) they are expected to change from their original values of Luo-Rudy model and Shannon model of ventricular myocytes; and 2) prior experimental studies suggested that they likely mediate the regulation of SR Ca<sup>2+</sup> clock ticking speed (67).

PKA has a relatively high activity in SANC (compared with myocytes) in the basal state, resulting in phosphorylation of phospholamban and RyRs (67), which enhance SR Ca<sup>2+</sup> pumping and affect SR Ca<sup>2+</sup> release, respectively.

We found that the isolated SR can indeed operate as a self-sustained Ca<sup>2+</sup> oscillator (53). An example of such an oscillator is shown in Fig. 2A, and its operation can be described by a simple "release-pumping-delay" mechanism: a small spontaneous Ca<sup>2+</sup> release from jSR to the subspace occurs as the primary or initiating event. When Ca<sup>2+</sup> in the subspace ( $Ca_{sub}$ ) increases to a sufficient level, it amplifies the Ca<sup>2+</sup> release via Ca<sup>2+</sup>-induced Ca<sup>2+</sup> release (CICR); this relatively strong, secondary Ca<sup>2+</sup> release simultaneously depletes (i.e., resets) jSR. The released Ca<sup>2+</sup> is pumped into the nSR. The delay between releases is determined by the Ca<sup>2+</sup> pumping rate and Ca<sup>2+</sup> diffusion from subspace to cytosol and also from nSR to jSR. As Ca<sup>2+</sup> in jSR ( $Ca_{jSR}$ ) slowly increases, RyRs are restituted, and the next release is ultimately initiated, etc.

### Dynamic Characteristics and Major Limitations of the Isolated SR Ca<sup>2+</sup> Oscillator

Our broad 2-D-parametric analysis of simultaneous  $k_s$  and  $P_{up}$  changes revealed that the SR Ca<sup>2+</sup> oscillations persist over a wide range of amplitudes and frequencies from 1.3 to 6.1 Hz (graded by red-white color in Fig. 2, B and C) that surpasses

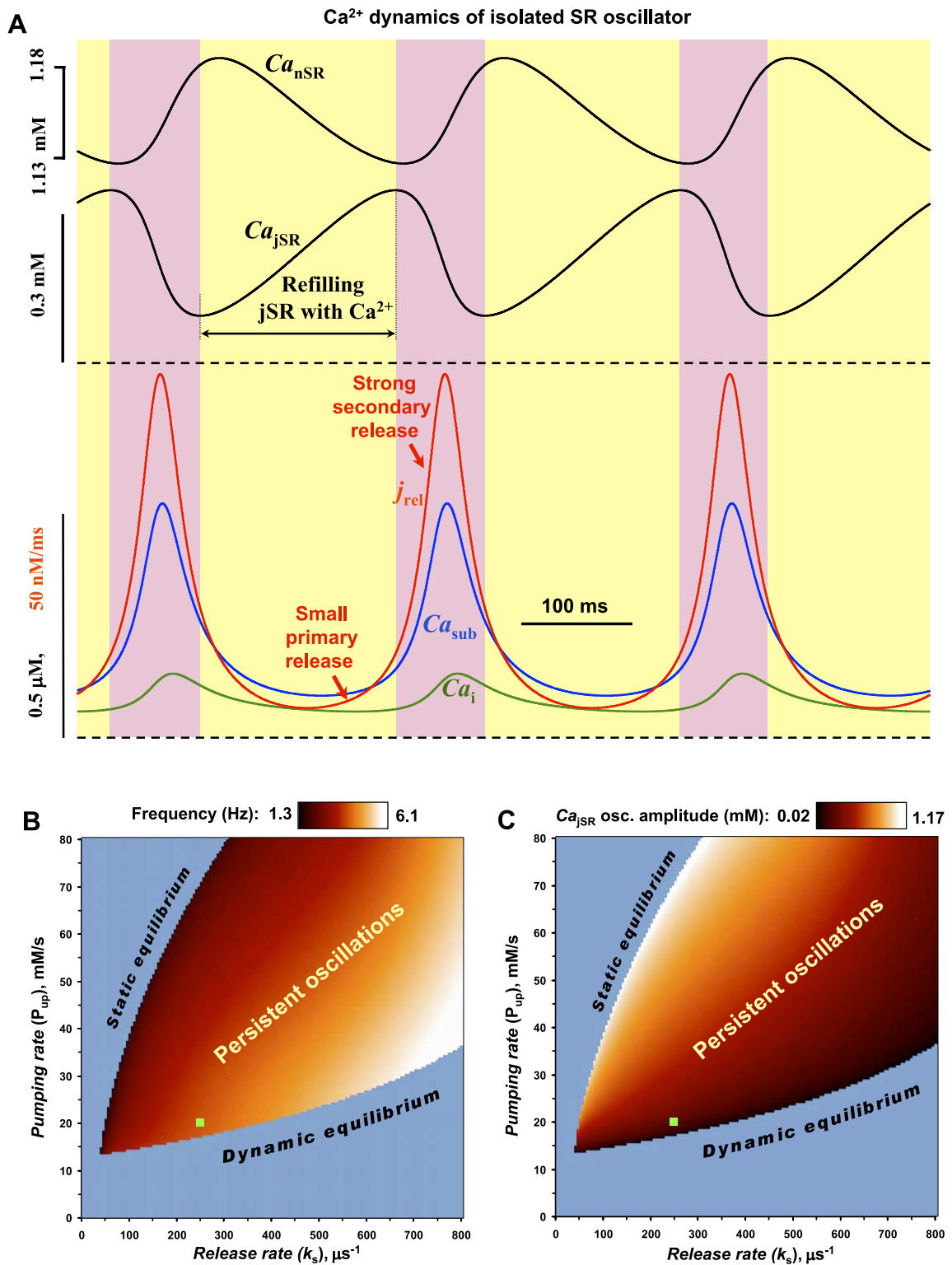


Fig. 2. Emergence and dynamic characteristics of the isolated  $\text{Ca}^{2+}$  SR oscillator (osc.) with a simple “release-pumping-delay” mechanism in our new model of rabbit SANC (all membrane currents = 0). A: model simulations illustrating that SR can operate as a self-sustained  $\text{Ca}^{2+}$  oscillator,  $P_{\text{up}} = 20$  mM/s. Note: for this and other simulations, we provide only those model parameters, which are different from our basal firing model, which is fully described in the online data supplement. B and C: results of parametric analysis for the isolated SR  $\text{Ca}^{2+}$  oscillator with simultaneously varying SR  $\text{Ca}^{2+}$  release rate and SR  $\text{Ca}^{2+}$  pumping rate are shown in terms of oscillation frequency (B) or amplitude (C). Each image shows the result of  $161 \times 161 = 25,921$  simulations (each pixel =  $5 \mu\text{s}^{-1} \times 0.5$  mM/s) with the resultant frequency or amplitude coded by the color map shown on each image top; the parametric space yielding no sustained  $\text{Ca}^{2+}$  oscillations is shown in blue. Small green box represents the  $\text{Ca}^{2+}$  oscillator shown in A.  $k_{\text{s}}$ , SR  $\text{Ca}^{2+}$  release rate constant.

the entire range of heart physiological rates. This extended range of rates of the  $\text{Ca}^{2+}$  oscillator is limited by bifurcation border of the cone in Fig. 2B. The highest rates are reached when the oscillator approaches to dynamic equilibrium (steady release) at the bottom border of the cone. The lowest rates are reached when the oscillator approaches to static equilibrium (no release) at the upper border of the cone.

Static equilibrium occurs when either the release rate is too small or  $\text{Ca}^{2+}$  pumping rate is too fast, i.e., jSR becomes highly loaded, but  $\text{Ca}_{\text{sub}}$  level is low and insufficient to induce secondary  $\text{Ca}^{2+}$  releases (Fig. 3C, left). A small steady background RyR release is well-balanced by  $\text{Ca}^{2+}$  pumping. The system behaves as a trigger in this instance: a short  $\text{Ca}^{2+}$  injection into subspace produces a strong  $\text{Ca}^{2+}$  transient via CICR (data not shown), similar to CICR in ventricular myocytes during an AP.

The oscillator behavior is simple—the higher its frequency, the less is its amplitude (Fig. 2, B vs. C)—and can be easily explained as  $\text{Ca}^{2+}$  release-pumping interplay in our simulations. Increasing  $k_s$  at a fixed  $P_{\text{up}}$  (Fig. 3, A and C) or decreasing  $P_{\text{up}}$  at a fixed  $k_s$  (Fig. 3B) boosts the oscillation frequency but simultaneously causes  $\text{Ca}^{2+}$  accumulation in the subspace ( $\text{Ca}_{\text{sub}}$  in Fig. 3C, solid traces) that facilitates subse-

quent CICR. In turn, the oscillation amplitude decreases as the maximum loading of jSR drops (Fig. 3C, dotted traces) because of less time available for the SR  $\text{Ca}^{2+}$  reloading. As  $k_s$  increases (or  $P_{\text{up}}$  decreases) further,  $\text{Ca}^{2+}$  is not removed sufficiently quickly from the subspace:  $\text{Ca}^{2+}$  oscillations become damped at high levels of  $\text{Ca}_{\text{sub}}$  with high, persistent  $\text{Ca}^{2+}$  release (Fig. 3C, right, "damped oscillator"). Thus, to sustain oscillations, a higher release rate must be matched with the faster  $\text{Ca}^{2+}$  removal from the subspace by faster pumping (Fig. 2, B and C, "Persistent oscillations").

The above-described paradigm, "the higher the rate, the lower the amplitude," represents the major limitation of the isolated  $\text{Ca}^{2+}$  oscillator: it is unable to generate high-amplitude oscillations at higher rates. Our further analysis will show that this problem is solved within the full (i.e., physiological) system of  $\text{Ca}^{2+}$  and membrane clocks.

#### Operation of Surface Membrane Clock within the System of Two Clocks

After we tuned parameters of the SR toward its experimentally observed  $\text{Ca}^{2+}$  oscillatory regime, we next explored the function of the system comprised of the membrane clock and

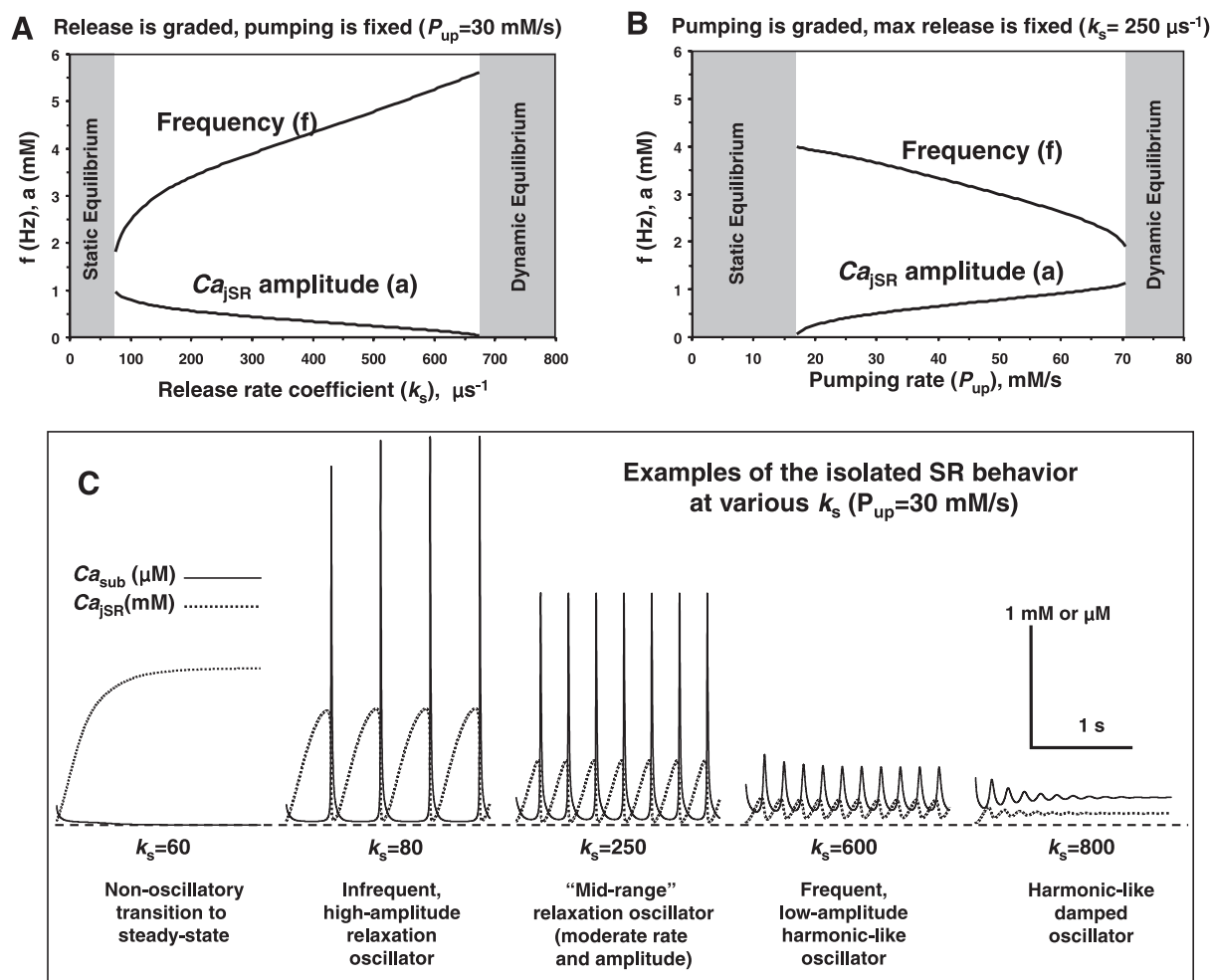


Fig. 3. A major limitation ("the faster, the weaker") of the isolated SR  $\text{Ca}^{2+}$  oscillator is its inability to sustain high-amplitude oscillations at high rates when  $k_s$  increases (A) or  $P_{\text{up}}$  decreases (B). C: model simulations at various  $k_s$  show that the mechanism of poor oscillator performance at high rates (i.e., decreasing amplitude) is linked to accumulation of  $\text{Ca}^{2+}$  in the submembrane space ( $\text{Ca}_{\text{sub}}$ , solid line). All membrane currents = 0.

the SR  $\text{Ca}^{2+}$  clock. Before our detailed parametric analysis, we first tested conceptually whether and how the membrane clock operates within such a system using an example of SR  $\text{Ca}^{2+}$  clock shown in Fig. 2A. Our simulations showed that membrane clock (Fig. 4, *top* traces) is indeed functional and apparently behaves in its well-known oscillatory pattern, as previously described (see review in Ref. 71). In short,  $I_{\text{CaL}}$  generates the AP upstroke, and rapid delayed rectifier current ( $I_{\text{Kr}}$ ; in rabbit) repolarizes the cell membrane. Inactivation of

$I_{\text{Kr}}$  produces an early DD phase, followed by contributions from activation of hyperpolarization-activated or “funny” current ( $I_{\text{f}}$ ), T-type  $\text{Ca}^{2+}$  current ( $I_{\text{CaT}}$ ), sustained current ( $I_{\text{st}}$ ),  $I_{\text{NCX}}$ , and sub-AP-threshold  $I_{\text{CaL}}$  during late DD. The cumulative action of these multiple DD mechanisms brings the membrane potential to the AP threshold, etc. Whereas our functional paradigm of SANC membrane clock includes well-known ion current types, their contributions, however, fundamentally differ from those in prior SANC models because of timely and strong

**Membrane clock**

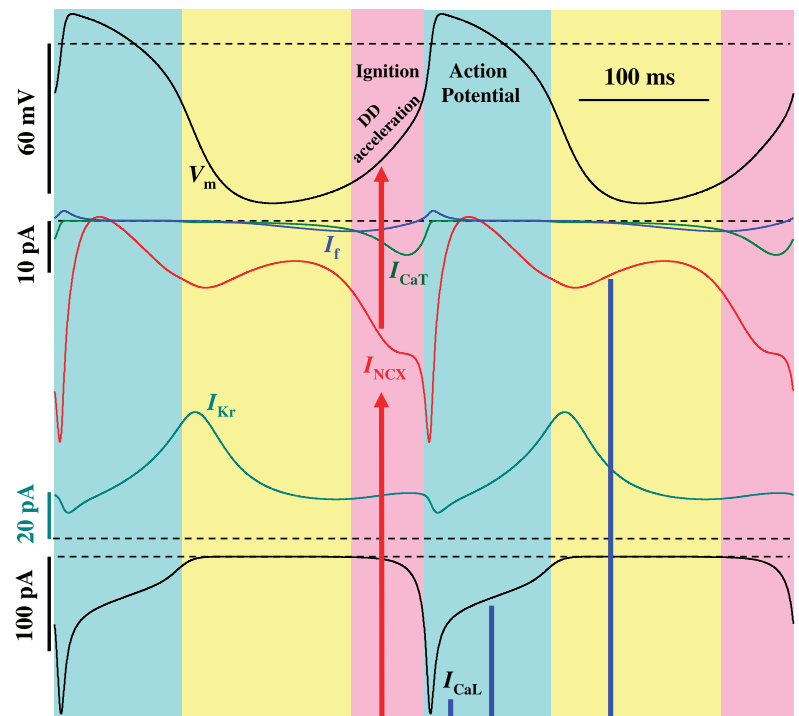
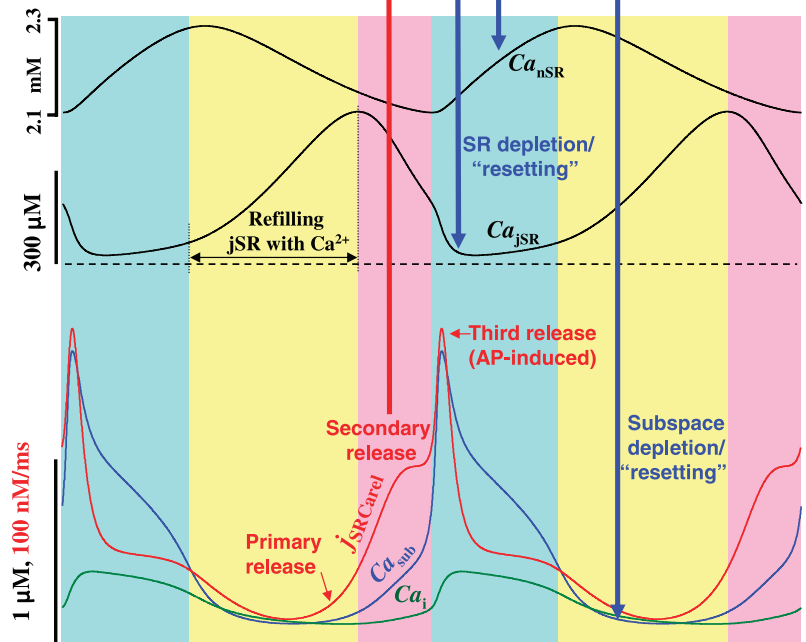


Fig. 4. Model simulations showing major dynamic interactions (vertical lines) of membrane clock and SR  $\text{Ca}^{2+}$  clock during spontaneous AP firing in rabbit SANC. Shown are simulated traces of voltage ( $V_m$ ), major ion currents,  $\text{Ca}^{2+}$  concentrations, and the  $\text{Ca}^{2+}$  release flux ( $j_{\text{SRCaRel}}$ ) during 2 pacemaker cycles. Dashed lines show 0 levels;  $P_{\text{up}} = 20 \text{ mM/s}$ . DD, diastolic depolarization.

**SR  $\text{Ca}^{2+}$  clock**



interactions of SR  $\text{Ca}^{2+}$  clock with membrane clock in our SANC model system (vertical arrows in Fig. 4).

#### Major Interactions of SR $\text{Ca}^{2+}$ Clock and Membrane Clock

SR  $\text{Ca}^{2+}$  and membrane clocks intimately interact biophysically and biochemically via coupling factors, such as  $\text{Ca}_{\text{sub}}$ , cAMP/PKA, and CaMKII, which influence function of both clocks (Fig. 5A). More specifically,  $I_{\text{CaL}}$  of membrane clock is modulated by high basal activities of CaMKII (69) and cAMP-dependent PKA (52, 67);  $I_{\text{CaL}}$  inactivation is accelerated by  $\text{Ca}_{\text{sub}}$ ;  $I_f$  is modulated by cAMP by shifting its voltage-dependent activation (12); and  $I_{\text{NCX}}$  is greatly increased by spontaneous intracellular  $\text{Ca}^{2+}$  releases (5). As to SR  $\text{Ca}^{2+}$  clock, its phospholamban, SR  $\text{Ca}^{2+}$  pump (SERCA), and RyRs are also modulated by  $\text{Ca}^{2+}$ , PKA, and CaMKII (Fig. 5A). The interactions of clocks via  $\text{Ca}_{\text{sub}}$  and cAMP/PKA result in robust generation of rhythmic APs in the model, as described below. Coupling via CaMKII was not specifically simulated here because of limited data in SANC (but see Refs. 33, 69).

We identified the essential interactions of SR  $\text{Ca}^{2+}$  clock and membrane clock by analyzing dynamics of the key com-

ponents of the system (Fig. 4). We also compared  $\text{Ca}^{2+}$  dynamics in the full system with those in the isolated SR  $\text{Ca}^{2+}$  clock (Fig. 4 vs. Fig. 2A, with SR having the same parameters).

1. AP ignition by  $I_{\text{NCX}}$  during late DD. Spontaneous primary releases during mid-DD, and then secondary releases during late DD occur in the full system as in isolated SR  $\text{Ca}^{2+}$  clock, but the secondary releases activate  $I_{\text{NCX}}$  (Fig. 4, vertical red arrows). This critical interaction, predicted by the model, is in good agreement with experimental results in rabbit SANC demonstrating that the late diastolic  $I_{\text{NCX}}$  is strongly activated by the occurrence of spontaneous local SR  $\text{Ca}^{2+}$  releases into the submembrane space (5). It has also been experimentally demonstrated that these spontaneous, local releases are, in fact,  $\text{Ca}^{2+}$  wavelets (5), which are driven by propagating CICR and described by secondary release in the model.  $I_{\text{NCX}}$  activation occurs at the critical phase of the pacemaker cycle, the late DD, when  $I_{\text{Kr}}$  and  $I_f$  DD mechanisms have faded out, but  $I_{\text{CaL}}$  is not yet appreciatively activated. Whereas  $I_{\text{NCX}}$ ,  $I_{\text{CaL}}$ ,  $I_{\text{CaT}}$ , and  $I_{\text{st}}$  contribute to the late DD,  $I_{\text{NCX}}$  contribution is the greatest in our model (Fig. 4) as demonstrated in experimental studies (4, 5, 74). DD acceleration via  $I_{\text{NCX}}$  activation brings the membrane to

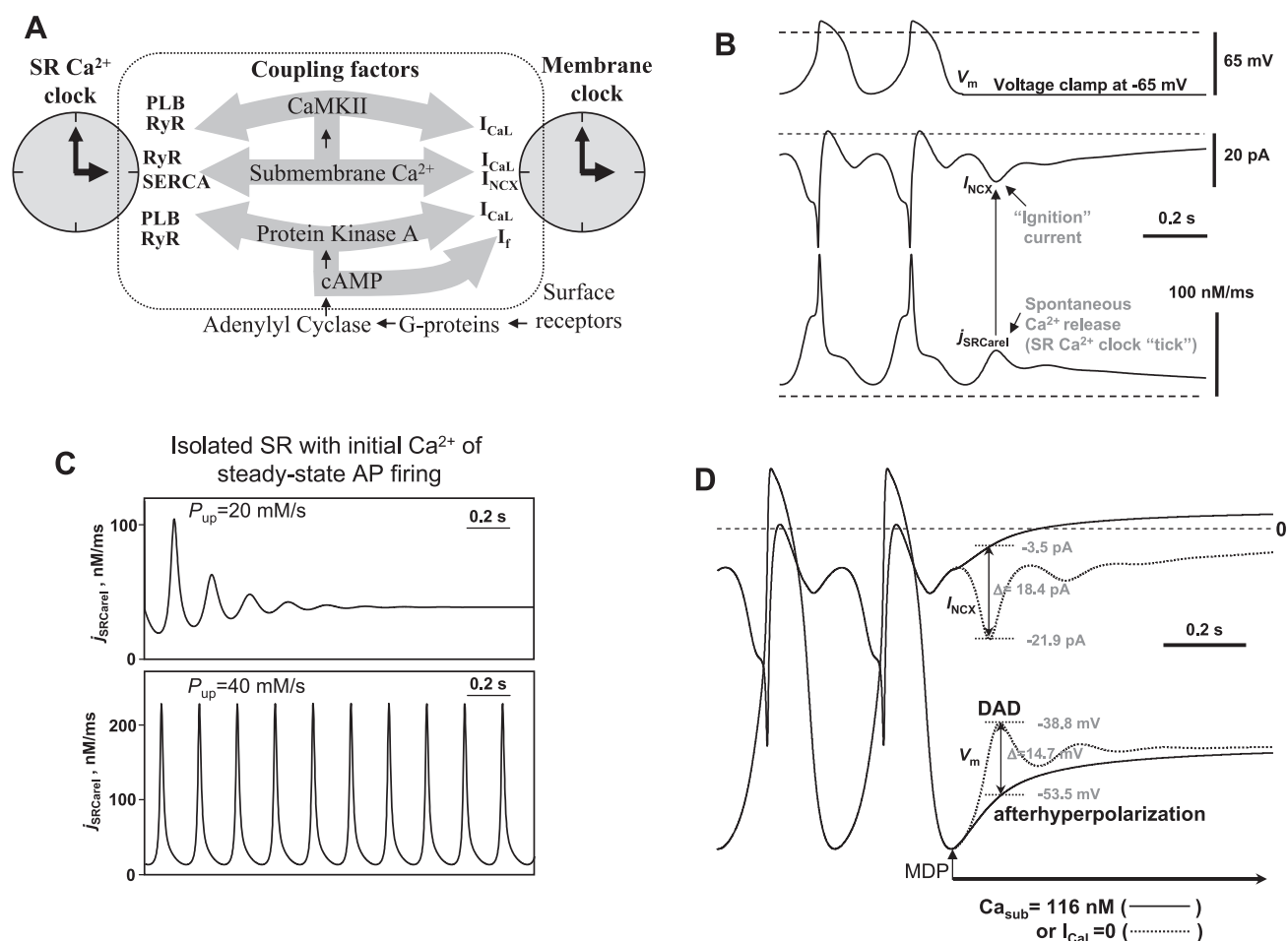


Fig. 5. Enhanced flexibility of the rate modulation in our model is based on mutual functional dependence of  $\text{Ca}^{2+}$  and membrane clocks. **A** illustrates factors that couple the 2 clocks comprising the novel pacemaker mechanism. **B**: damped SR  $\text{Ca}^{2+}$  release oscillations and  $I_{\text{NCX}}$  oscillations when membrane clock is instantly disabled by a voltage clamp to  $-65$  mV;  $P_{\text{up}} = 20$  mM/s. **C**: different patterns of  $\text{Ca}^{2+}$  release dynamics at different  $P_{\text{up}}$  of 20 and 40 mM/s in the isolated  $\text{Ca}^{2+}$  SR oscillator (all membrane currents = 0), simulated with the initial cell  $\text{Ca}^{2+}$  load of steady-state AP firing such as shown Fig. 4. The steady oscillations at 40 mM/s are shown after 40 s of simulated SR activity. **D**: simulations of  $V_m$  and  $I_{\text{NCX}}$  dynamics when  $\text{Ca}_{\text{sub}}$  was fixed at the maximum diastolic potential (MDP) (solid curves) or when  $I_{\text{CaL}}$  was completely blocked at the MDP (dotted curves), resulting in afterhyperpolarization or delayed afterdepolarization (DAD), respectively;  $P_{\text{up}} = 20$  mM/s.

its excitation threshold and thereby basically ignites rhythmic spontaneous APs (Fig. 4, “DD acceleration”). Acceleration of late DD by  $I_{\text{NCX}}$  was also demonstrated experimentally in rabbit SANC (4, 5).

2. *SR depletion/resetting.* Compared with  $\text{Ca}^{2+}$  dynamics of isolated SR  $\text{Ca}^{2+}$  clock (Fig. 2A), the full system generates additional  $\text{Ca}^{2+}$  release that occurs during AP via the conventional  $I_{\text{CaL}}$ -related CICR (Fig. 4, “Third release”), resulting in conventional  $\text{Ca}^{2+}$  transient and strong jSR depletion, resetting SR  $\text{Ca}^{2+}$  cycling. In contrast to a relatively slow SR “self-resetting” (Fig. 2A),  $I_{\text{CaL}}$  resets SR quicker and more efficiently as it almost instantly boosts  $\text{Ca}_{\text{sub}}$  (Fig. 4,  $\text{Ca}_{\text{sub}}$  blue trace).

3. *SR refueling.* Isolated  $\text{Ca}^{2+}$  clock (Fig. 2A) has a fixed total amount of  $\text{Ca}^{2+}$  that is defined by the model operator, which chooses initial conditions for simulations (mainly by the initial  $\text{Ca}_{\text{nSR}}$  level). However, when the SANC model is spontaneously firing rhythmic APs, the amount of  $\text{Ca}^{2+}$  in the system (the “fuel”) is mainly determined by the balance of  $\text{Ca}^{2+}$  efflux by NCX and influx by  $I_{\text{CaL}}$ . In other words, the system of interacting SR and sarcolemma tunes and equilibrates a specific appropriate amount of cell  $\text{Ca}^{2+}$  at a given rate. For example, the full system in Fig. 4 tunes its  $\text{Ca}_{\text{nSR}}$  to  $\sim 2.2$  mM, that is  $\sim 63\%$  higher than it was set initially in the system (1.35 mM; see Table 1). Refueling/reloading the  $\text{Ca}^{2+}$  cycling is achieved during the AP, as  $\text{Ca}^{2+}$  influx of  $I_{\text{CaL}}$  is made available for pumping into nSR (Fig. 4, SR “refueling”).

4. *Subspace depletion/resetting.* NCX assists SR  $\text{Ca}^{2+}$ -ATPase in  $\text{Ca}^{2+}$  removal from the subspace, including during the DD, so that  $\text{Ca}_{\text{sub}}$  declines after AP to the levels that are below than the  $\text{Ca}^{2+}$  in bulk cytosol ( $\text{Ca}_i$ ) (Fig. 4, bottom, right blue arrow). In contrast, when SR  $\text{Ca}^{2+}$  clock operates without the membrane clock,  $\text{Ca}_{\text{sub}}$  remains always higher than  $\text{Ca}_i$  (Fig. 2A). This NCX-assisted “cleanup” of  $\text{Ca}^{2+}$  in subspace during early and mid-DD delays the  $\text{Ca}_{\text{sub}}$  increase caused by primary  $\text{Ca}^{2+}$  release and thereby prevents premature secondary  $\text{Ca}^{2+}$  release in our model. This, in turn, gives sufficient time to reload jSR to higher levels, culminating in strong synchronized spontaneous release during later DD and larger  $\text{Ca}^{2+}$  oscillation amplitude (e.g., 472 vs. 255  $\mu\text{M}$  for  $\text{Ca}_{\text{jSR}}$  oscillation amplitude in Fig. 4 vs. Fig. 2A).

### The Concept of System $\text{Ca}^{2+}$ Clock

Thus a major result of our analysis so far is that a reductionist approach separating functional paradigm of either clock makes no sense for the physiological system of strongly coupled oscillators during spontaneous AP firing. The two oscillators tune their operation and phases toward mutually entrained operation so that they operate in antiphase (spontaneous release  $\rightarrow$  AP  $\rightarrow$  spontaneous release, etc.). In this instance, the  $\text{Ca}^{2+}$  clock paradigm is not limited to the SR  $\text{Ca}^{2+}$  cycling but also includes SR-sarcolemma interactions. Thus the system  $\text{Ca}^{2+}$  clock (or physiological  $\text{Ca}^{2+}$  clock; “System  $\text{Ca}^{2+}$  clock” in Fig. 1) in addition to its SR  $\text{Ca}^{2+}$  loop (“SR  $\text{Ca}^{2+}$  clock” in Fig. 1) also includes the sarcolemmal  $\text{Ca}^{2+}$  loop (bold arrows in Fig. 1) formed by function of  $\text{Ca}^{2+}$  channels and NCX.

The importance of this additional loop for  $\text{Ca}^{2+}$  cycling is easily tested in our model by an instant voltage clamp to  $-65$  mV. These conditions halt activation of voltage-dependent ion currents and their balanced sarcolemmal  $\text{Ca}^{2+}$  fluxes. If those

fluxes were minor for the system  $\text{Ca}^{2+}$  clock function,  $\text{Ca}^{2+}$  oscillations would persist similarly to that shown in Fig. 2A. However, our model predicts that the  $\text{Ca}^{2+}$  clock with instantly disrupted physiological links damps after a few oscillations rather than persists (Fig. 5B). This model prediction recapitulates prior experimental findings in rabbit SANC of the damped oscillatory submembrane  $\text{Ca}^{2+}$  signals under voltage clamp at  $-65$  mV (70).

Since cell  $\text{Ca}^{2+}$  load is critically important for function of  $\text{Ca}^{2+}$  clock, another method to test the importance of the membrane  $\text{Ca}^{2+}$  loop is to compare function of SR  $\text{Ca}^{2+}$  clock and the system  $\text{Ca}^{2+}$  clock under the same  $\text{Ca}^{2+}$  load that is achieved during steady-state AP firing shown in Fig. 4. We calculated steady-state averages for  $\text{Ca}^{2+}$  in all four cell compartments: cytosol ( $\text{Ca}_i = 219$  nM), submembrane space ( $\text{Ca}_{\text{sub}} = 456$  nM), jSR ( $\text{Ca}_{\text{jSR}} = 0.217$  mM), and nSR ( $\text{Ca}_{\text{nSR}} = 2.2$  mM), represented by variables  $y_1$ – $y_4$  in Table 1. A given steady-state was insured by our standard criterion (see METHODS) of  $<0.01\%$  change (cycle to cycle) in AP amplitude and cycle length. All four steady-state averages were then used as initial conditions for respective variables in new simulations of the isolated SR  $\text{Ca}^{2+}$  dynamics (all sarcolemmal currents were set to 0). As a result, we got damping of  $\text{Ca}^{2+}$  oscillations (Fig. 5C, top), a response basically similar to that obtained with instant voltage clamp to  $-65$  mV (Fig. 5B). We also found that steady  $\text{Ca}^{2+}$  oscillations of isolated SR under these cell  $\text{Ca}^{2+}$  loading conditions are still possible but require a substantial  $P_{\text{up}}$  increase from 20 to  $>29$  mM/s (Fig. 5C, bottom). Thus these simulations provided additional evidence for our concept of the full system  $\text{Ca}^{2+}$  clock: although isolated SR can persistently oscillate any given  $\text{Ca}^{2+}$  load with a respective increase in  $P_{\text{up}}$ , the synergism of SR and sarcolemma within entire SANC pacemaker system allows robust  $\text{Ca}^{2+}$  oscillations at much lower (i.e., physiologically reasonable)  $P_{\text{up}}$  values.

### *Ca<sup>2+</sup> Clock Confers System Flexibility: the AP Firing Rate is Broadly Modulated by the Ca<sup>2+</sup> Clock Ticking Speed*

Although the system  $\text{Ca}^{2+}$  clock clearly depends on sarcolemmal  $\text{Ca}^{2+}$  fluxes, the critical late DD  $\text{Ca}^{2+}$  signals are still generated by spontaneous SR  $\text{Ca}^{2+}$  releases. Simulations under voltage clamp at  $-65$  mV (Fig. 5B) revealed the true spontaneous nature of these releases and their  $I_{\text{NCX}}$  counterparts/spikes at the time of late DD (“would-be” DD). Next, we evaluated the “power” of those NCX spikes, i.e., how much depolarization they can produce in our model. We compare membrane depolarizations and  $I_{\text{NCX}}$  in two simulations: 1) when  $\text{Ca}_{\text{sub}}$  was instantly fixed at its maximum diastolic potential (MDP) level of 116 nM (no  $\text{Ca}^{2+}$  release); and 2) when  $I_{\text{CaL}}$  was inhibited also at MDP (Fig. 5D). In its essence, the first simulation (solid trace in Fig. 5D) shows a smooth afterhyperpolarization without ignition, and the second simulation (dotted trace in Fig. 5D) shows an oscillatory delayed afterdepolarization produced by the oscillatory spontaneous release on the top of this afterhyperpolarization. The  $I_{\text{NCX}}$  difference at its first peak was 18.4 pA, and depolarization difference was 14.7 mV. Thus  $\text{Ca}^{2+}$  release-induced  $I_{\text{NCX}}$  spikes are sufficient to timely bring the membrane potential to  $-38.8$  mV, i.e., well above  $I_{\text{CaL}}$  activation threshold, from the level of afterhyperpolarization ( $-53$  mV) reached by the early

and mid-DD mechanisms (mainly  $I_{Kr}$  inactivation and activation of  $I_f$  and  $I_{CaT}$ ). Prior experimental studies showed that an ion current of only a few picoamperes scale can indeed drive the critical DD phase (11). Thus the spontaneous  $Ca^{2+}$  releases can be interpreted as  $Ca^{2+}$  clock ticks and their NCX spikes as ignition currents. Our model simulations thus support ideas about importance of late DD and  $I_{NCX}$  for cardiac cell pacemaker function in general (55, 74) and for function of rabbit SANC specifically (4, 5).

We then numerically tested an hypothesis that grading  $Ca^{2+}$  clock ticking speed strongly modulates the AP firing rate in our model. Grading  $P_{up}$  from 1 to 40 mM/s, indeed, greatly (2.3-fold) increased the AP firing rate from 1.8 to 4.2 Hz (Fig. 6A). Our additional simulations (Fig. 7) revealed the mechanism of the broad rate modulation by  $P_{up}$ , which includes coordinated changes of phase and amplitude for the diastolic  $Ca^{2+}$  release (i.e.,  $Ca^{2+}$  clock ticks; Fig. 7C). At higher pumping rates, both the amplitude and the frequency of  $Ca^{2+}$  oscillations increase due to a substantial shift in the net cell  $Ca^{2+}$  balance:  $I_{CaL}$  is

activated more frequently, resulting in a larger net  $Ca^{2+}$  influx. This larger  $Ca^{2+}$  influx combined with faster pumping increases the average  $Ca_{nSR}$  level (Fig. 7A) and rate of jSR refilling (Fig. 7B). Higher jSR  $Ca^{2+}$  loads are achieved in shorter times (Fig. 7B), thereby insuring larger amplitude of diastolic  $Ca^{2+}$  release (Figs. 6B and 7C) and larger NCX currents (i.e., ignition currents; Fig. 7D) to quickly bring membrane potential to AP excitation threshold, i.e., to ignite APs (Fig. 7E). Larger NCX currents, in turn, simultaneously balance increased  $Ca^{2+}$  influx via  $I_{CaL}$ .

The interactions of SR and sarcolemma described above overcome the major limitation of the isolated SR  $Ca^{2+}$  clock, i.e., its inability to sustain high-amplitude oscillations at high rates (i.e., “the faster, the weaker”; Fig. 3). In contrast, the oscillation amplitude of the full system  $Ca^{2+}$  clock raises as the oscillation rate increases (i.e., “the faster, the stronger”; Fig. 6B, inset).

#### Finding the System Solution for the Basal State AP Firing by Interacting Clocks

Since  $P_{up}$  modulates AP firing rate so smoothly and broadly (Fig. 6A), the  $P_{up}$ -AP rate modulation curve yields a unique parametric solution basically for any given reasonable value of the basal AP firing rate. A conventional, mid-range AP basal rate of 3 Hz measured in rabbit SANC (Table 2) is reached in our model somewhere in the middle of the most effective, almost linear range (1–25 mM/s) of rate modulation by  $P_{up}$ . The respective unique parametric solution of  $P_{up} = 12$  mM/s for this basal rate (3 Hz) is shown in Fig. 6A by black circle. This solution is further explored as basal state firing SANC model.

#### Major Electrophysiological Characteristics of Basal Firing SANC Model

Basic AP characteristics (Table 2) of our basal AP firing model are within the range of experimental data and similar to those of previous SANC models. Predictions for major ion current densities during spontaneous SANC firing for different models are listed in Table 3. Our model has typical densities for  $I_f$  and  $I_{CaL}$ . Its predictions for  $I_{CaT}$  and  $I_{st}$  densities are smaller than some but not all prior models; our values for these currents are reasonable, given the experimental facts: 1)  $I_{CaT}$  was detected only in 20% of SANC (in 5 of 25 cells tested; Ref. 44), and its experimental blockade has small effect on the spontaneous beating rate (see review in Ref. 71); and 2) molecular origin and specific blockers for  $I_{st}$  have not yet been identified;  $I_{st}$ , in fact, exhibits many properties of  $I_{CaL}$  and  $I_{NCX}$  and, therefore, may not be a discrete entity. Furthermore,  $I_{st}$  is not incorporated in many classic models (71), including the Kurata model (Ref. 27; its version with  $I_{st} = 0$ ). A larger density of the late diastolic  $I_{NCX}$  in our model is related to NCX activation by spontaneous diastolic  $Ca^{2+}$  release ( $Ca^{2+}$  clock ticks, discussed above). This larger diastolic  $I_{NCX}$  density of 0.458 pA/pF is within experimental estimates of the ryanodine-sensitive current during DD from 0.3 pA/pF (68) to 1.6 pA/pF (5). Whereas the Kurata model also predicts substantial diastolic  $I_{NCX}$  (0.328 pA/pF; Table 3), its time course is fundamentally different from that in our model (Fig. 8). The  $I_{NCX}$  dynamic in Kurata model (Fig. 8, dotted lines) exhibits a

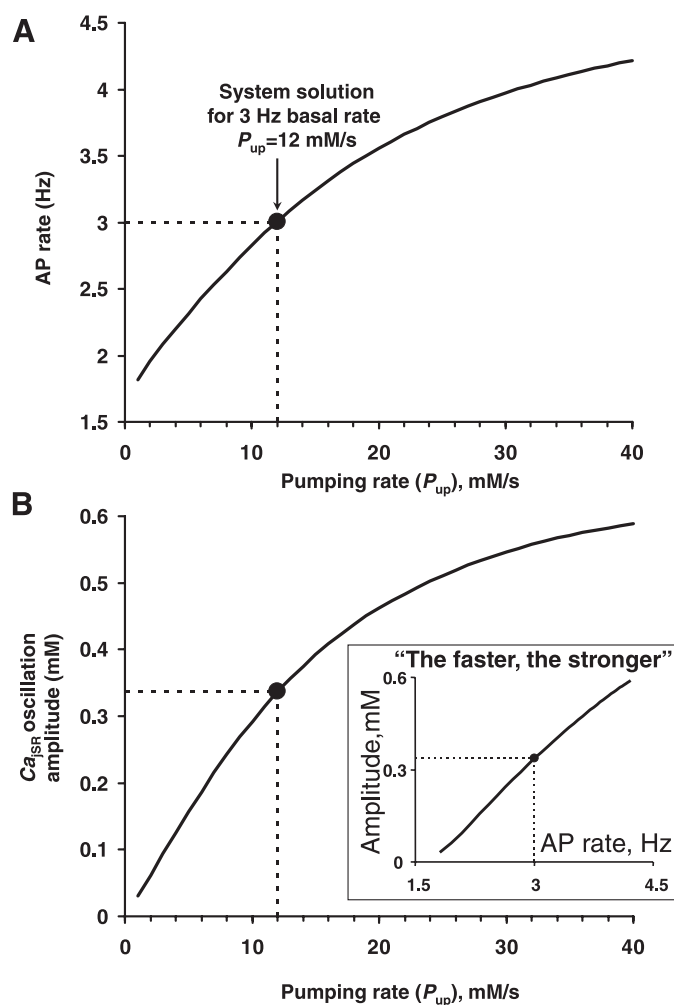


Fig. 6. A: the AP firing rate is broadly and smoothly modulated by  $P_{up}$ , yielding a unique parametric solution for the 3-Hz basal AP rate (black circle). B: interactions of  $Ca^{2+}$  and membrane clocks result in higher amplitude  $Ca^{2+}$  oscillations at higher  $P_{up}$  values. Since higher  $P_{up}$  values result in higher AP rates (A), the system clock operates following a Bowditch-like pattern: “the faster rate, the stronger release” (inset) thus overcoming a major functional limitation of the isolated SR  $Ca^{2+}$  clock (“the faster, the weaker” in Fig. 3).

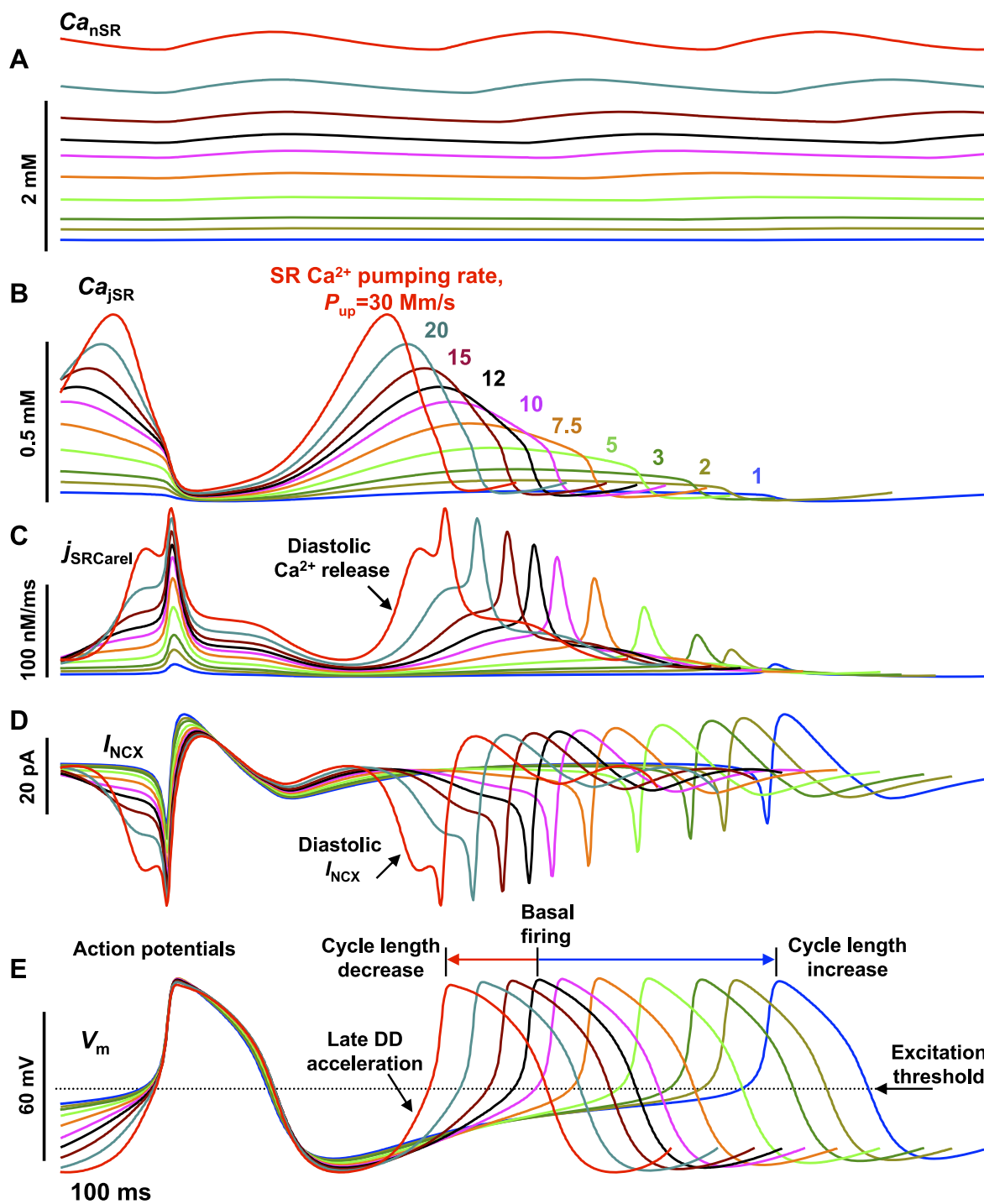


Fig. 7. The mechanism of broad spontaneous AP rate modulation by  $P_{up}$ . Overlapped traces are simulations for  $Ca_{nSR}$  (A),  $Ca_{jSR}$  (B),  $j_{SRCarel}$  (C),  $I_{NCX}$  (D), and  $V_m$  (E) at various  $P_{up}$  (labels in B). Simulations at different  $P_{up}$  are shown by different colors. All traces were synchronized with the 1st AP crossing 0 mV at the same time (100 ms) and reasonably time-truncated to illustrate phase shifts. See text for details.

decrease followed by a plateau throughout almost the entire DD; the subsequent  $I_{NCX}$  surge during the AP upstroke is driven by  $I_{CaL}$  activation and a conventional AP-induced  $Ca^{2+}$  transient. In contrast, the  $I_{NCX}$  dynamic in our model exhibits substantial increase throughout the mid- to late DD, i.e., clearly before  $I_{CaL}$  activation (Fig. 8, solid lines). This  $I_{NCX}$  increase is driven by spontaneous diastolic  $Ca^{2+}$  release from SR (Fig. 7C) that is also observed in experimental studies of rabbit

SANC (5, 68) but missing in the original Kurata model. It is important to note that it is ion current dynamics (i.e., the change in ion current balance), rather than just ion current instant values, that drive the DD. For example, although  $K^+$  delayed rectifier current has an outward direction, it greatly contributes to the early DD when its conductance inactivates (46). Thus the strongly increasing  $I_{NCX}$  during DD is a major unique feature of our basal firing model that makes it superior in predicting numerous, highly

Table 2. Basic AP characteristics of our basal firing model (in bold) are similar to those of some previous SANC models and within experimental data

Characteristics	Noble and Noble (49) Central SANC Model	Zhang et al. (73) Central SANC Model	Demir et al. (10) SANC Model	Kurata et al. (27) Central SANC Model	Present Model of Central SANC	The Range of Experimental Values
MDP, mV	-61	-58	-61	-59	<b>-62.7</b>	-66.2 to -51.9
APA, mV	84	79	96	75	<b>75.9</b>	66-78
CL, ms (AP rate, Hz)	263 (3.8)	327 (3.06)	263 (3.8)	307.5 (3.26)	<b>333 (3)</b>	247-389 (2.6-4.1 Hz)
APD <sub>50</sub> , ms	70	139	86	107	<b>101</b>	72.7-111
dV/dt <sub>max</sub> , V/s	4.7	2.7	9.6	6.4	<b>4.8</b>	4.8-27

All data for prior models were taken from Table 3 in Ref. 71. The ranges of experimental values were evaluated based on data in Table 1 in Ref. 27 (compiled from 12 studies that used physiological temperatures). MDP, maximum diastolic potential; APA, action potential (AP) amplitude; APD<sub>50</sub>, AP duration at its half amplitude; dV/dt<sub>max</sub>, the maximum rate of rise of membrane potential during AP upstroke; CL, cycle length.

reproducible experimental findings related to Ca<sup>2+</sup> cycling and its interaction with the sarcolemma in SANC.

#### Basal Firing Model Predicts Effects of Experimental Inhibition of Ca<sup>2+</sup> Clock, NCX, and I<sub>f</sub>

**Effect of SR Ca<sup>2+</sup> pump inhibition.** Two recent pharmacological studies (56, 66) provided new, direct evidence of the importance of SR Ca<sup>2+</sup> cycling kinetics for basal rate in SANC. In both studies, inhibition of SR Ca<sup>2+</sup> pump by cyclopiazonic acid (CPA) resulted in substantial decrease of SANC beating rate by 30% (guinea pig) and 26% (rabbit), respectively. Inhibition of Ca<sup>2+</sup>-ATPase by CPA in rabbit SANC can be easily interpreted and tested in our model in terms of a reduction in the SR Ca<sup>2+</sup> pumping rate, P<sub>up</sub>. The P<sub>up</sub>-AP rate modulation curve predicted by our model extends to very low rates, down to 1.8 Hz, i.e., 40% decrease (Fig. 9A) from its basal rate value of 3 Hz. Thus our parametric (P<sub>up</sub>) analysis yields a unique solution for the CPA (3 μM) experimental result, with P<sub>up</sub> decreasing to 4 mM/s, i.e., to approximately one-third of its basal value of 12 mM/s (Fig. 9A, "Present model"). An example of model simulation for the CPA effect is shown in Fig. 9B. It is important to note that this prediction is an example of the unique property of our new model, i.e., the model exhibits a distinguishably wide range of rate modulation by Ca<sup>2+</sup> cycling. All prior SANC models have extremely narrow (if any) rate modulation by SR Ca<sup>2+</sup> pumping and therefore have no solution for the experimental CPA effect. For example, as shown in Fig. 9A, Zhang et al. (73) model has no equations for Ca<sup>2+</sup> cycling; the Kurata model predicts almost negligible (only 3.5%) rate decrease on complete SR Ca<sup>2+</sup> pump inhibition; and, paradoxically, the Kyoto model of guinea pig SANC (57) predicts a slight AP rate increase rather than decrease as SR Ca<sup>2+</sup> pump is inhibited.

**Effect of short-term inhibition of NCX by lithium.** Our basal state model reproduces the effect of the "skipped" AP on a

short-term experimental inhibition of NCX by a rapid and brief substitution of Li<sup>+</sup> for Na<sup>+</sup> (lithium spritz; Ref. 5; Fig. 9C).

**Effect of large concentrations of ryanodine.** It is widely accepted that ryanodine, which interferes with normal SR Ca<sup>2+</sup> release, slows basal AP firing rate of rabbit SANC. Depending on its concentration and time after administration, the range of the effect varies from moderate AP rate slowing to complete halt (reviewed in Ref. 30). The most recent study by Lyashkov et al. (37) showed that spontaneous AP firing fails in 83% of cells after 15 min at a high ryanodine concentration of 30 μM. In line with this experimental result, our basal state model fails to generate rhythmic APs when SR Ca<sup>2+</sup> cycling is completely inhibited (Fig. 9D). This is another example illustrating that Ca<sup>2+</sup> and membrane clocks are strongly coupled during basal AP firing: once rhythmic ignition currents initiated by Ca<sup>2+</sup> clock are halted, membrane clock undergoes a lengthy transitional process including subthreshold oscillations, which eventually generate dysrhythmic excitations.

**Modest effect of I<sub>f</sub> blockade by Cs<sup>+</sup>.** In our basal model, blockade of I<sub>f</sub> (Fig. 9E) results in the rate reduction by 5.0%, i.e., close to 5.2% measured experimentally in single rabbit SANC when I<sub>f</sub> was blocked by Cs<sup>+</sup> (65).

#### Ca<sup>2+</sup> Clock Confers the System Robustness

Next, we tested a hypothesis that clock interactions enhance robustness of the SANC pacemaker system. For this purpose, we examined the system behavior on simultaneous variations of key system parameters of P<sub>up</sub> and g<sub>CaL</sub>. This analysis (Fig. 10A) identified P<sub>up</sub>-g<sub>CaL</sub> areas of rhythmic APs, chaotic APs, and no firing of the entire system. The areas of both chaotic firing and no firing greatly narrow toward lower g<sub>CaL</sub> values as P<sub>up</sub> rises, and, vice versa, gradually increasing g<sub>CaL</sub> extends the P<sub>up</sub> range of rhythmic firing. As defined in METHODS, the larger the

Table 3. Amplitudes of ion currents [contributing to mid- to late diastolic depolarization (DD)] predicted by our basal firing model (in bold) compared with some previous SANC models

Characteristics	Noble and Noble (49) Central SANC Model	Zhang et al. (73) Central SANC Model	Demir et al. (10) SANC Model	Kurata et al. (27) Central SANC Model	Present Model of Central SANC
Maximum diastolic I <sub>f</sub> , pA/pF	0.061	0.1	0.073	0.109	<b>0.068</b>
Maximum I <sub>CaT</sub> , pA/pF	No I <sub>CaT</sub>	0.353	0.188	0.227	<b>0.09</b>
Maximum peak I <sub>CaL</sub> , pA/pF	4.95	3.46	11.00	6.87	<b>5.35</b>
Maximum peak I <sub>st</sub> , pA/pF	No I <sub>st</sub>	No I <sub>st</sub>	No I <sub>st</sub>	0.40	<b>0.1</b>
Late diastolic I <sub>NCX</sub> , pA/pF	0.06	0.03	0.15	0.328	<b>0.458</b>

Late diastolic Na<sup>+</sup>-Ca<sup>2+</sup> exchanger current (I<sub>NCX</sub>; bottom row) was measured at 85% of cycle length from the upstroke at 0 mV of the prior AP (e.g., Fig. 8, I<sub>NCX</sub>). The current densities of previous models were estimated from simulations presented in review by Wilders (71).

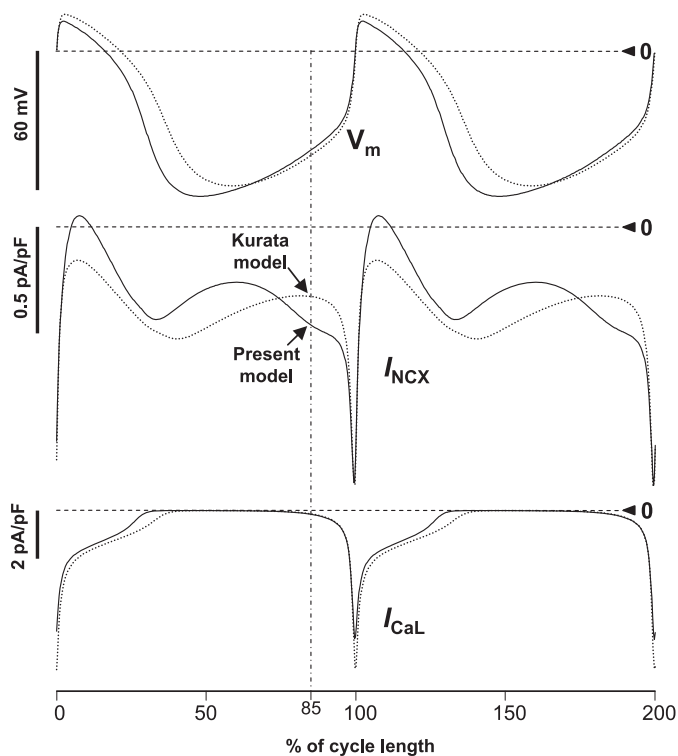


Fig. 8. In contrast to Kurata model (dotted curves), our basal firing model ("Present model," solid curves) exhibits strong increase of inward  $I_{NCX}$  during diastolic depolarization before activation of  $I_{CaL}$ . Simulated dynamics of membrane potential ( $V_m$ ),  $I_{NCX}$ , and  $I_{CaL}$  at a steady-state AP firing are shown for 2 pacemaker cycles beginning at  $V_m = 0$ . The cycle lengths were 307.5 and 333 ms for Kurata model and our basal model, respectively. The vertical dash-dot line of 75% of cycle length illustrates approximate timing for  $I_{CaL}$  activation, i.e., when  $I_{NCX}$  was measured in Table 3.

parameter variations, in the absence of the system performance compromise, define the more robust system. Thus our analysis shows that although the membrane-delimited clock (at  $P_{up} = 0$ , i.e., along the abscissa) can indeed generate rhythmic APs within a limited  $g_{CaL}$  range, the system of  $Ca^{2+}$  and membrane clocks is more robust because the combined system greatly performs in the range of low  $g_{CaL}$  values, where the classic membrane-delimited clock fails. For example, at  $P_{up} = 12$  mM/s, the system is able to generate rhythmic APs at extremely low  $I_{CaL}$  conductances, down to 0.295 nS/pF (green dash line); but when the  $Ca^{2+}$  clock is disabled ( $P_{up} = 0$ ), the cell membrane needs a substantial (58.5%) increase of its  $I_{CaL}$  conductance to 0.4675 nS/pF for spontaneous APs just to emerge (on the right of the red dash line in Fig. 10A). Also, whereas the full system generates high-quality frequent APs at various  $g_{CaL}$ , the membrane clock operating alone halts, generates chaotic APs, or greatly slows (Fig. 10B).

Next, we compared the results of  $g_{CaL}$ - $P_{up}$  parametric analysis at different  $I_f$  conductances ( $g_{If}$ ). This comparison revealed that although  $I_f$  provides only small contribution to basal firing (Fig. 9E), it greatly increases the area of rhythmic firing, especially at low rates (along the entire border line of rhythmic firing in Fig. 11) and thus also greatly enhances the system robustness. Thus our overall parametric analysis for simultaneous changes of  $g_{If}$ ,  $g_{CaL}$ , and  $P_{up}$  (Figs. 10 and 11) reveals that the existence of strong interactions of respective multiple pacemaker mechanisms (i.e.,  $I_{CaL}$ ,  $I_f$ , and  $I_{NCX}$

activated by  $Ca^{2+}$  clock) greatly enhances the robustness of the coupled SANC pacemaker system. Specifically, any enhancement of either mechanism broadens the fail-safe ranges for the other two mechanisms (Figs. 10 and 11): 1) increasing  $P_{up}$  broadens fail-safe changes for  $g_{CaL}$  and  $g_{If}$ ; 2) increasing  $g_{CaL}$  broadens fail-safe changes for  $g_{If}$  and  $P_{up}$ ; and 3) increasing  $I_f$  broadens fail-safe changes for  $g_{CaL}$  and  $P_{up}$ .

#### High $I_{CaL}$ and $I_f$ Conductances Limit Pacemaker Flexibility

The results and logic of the above section lead, however, to an apparent paradox. The natural evolution of the pacemaker system has somehow culminated in a less robust membrane clock, whereas its higher robustness could be very easily achieved by a simple increase in  $g_{CaL}$  and/or  $g_{If}$ , e.g., an additional  $Ca^{2+}$  channel and/or  $f$ -channel expression. To solve the paradox, we asked the question, "what might be an additional functional advantage of our modeled coupled clock system with a moderate  $g_{CaL}$  and/or  $g_{If}$  vs. a system with very high  $g_{CaL}$  and/or  $g_{If}$ ?" Our model simulations show that the range of rate regulation by  $P_{up}$  substantially shrinks as  $g_{CaL}$  or  $g_{If}$  increases (Fig. 12). We interpret this result as follows: although higher  $g_{CaL}$  or  $g_{If}$  enhances the system robustness, this substantially limits the flexibility of the pacemaker function (at least via  $P_{up}$  modulation). Thus the experimental data (e.g., ryanodine effect) show, and our new model validates the experimental data, that the real SANC membrane clock operating alone is more fragile compared with that portrayed by previous essentially membrane-delimited SANC models (all those models had no or little dependence on  $Ca^{2+}$  cycling); but, at the same time, the coupled clock system is very robust and, importantly and advantageously, also very flexible. In other words, the membrane clock seems to forgo some its high robustness to allow the smooth and wide range of rate regulation via interactions of  $Ca^{2+}$  clock and membrane clock. "In return" the  $Ca^{2+}$  clock greatly enhances (i.e., recovers) the coupled system robustness (Fig. 10A) so that the coupled system likely achieves the highest possible balance of robustness and flexibility that is critical for effective pacemaker function (and thus for survival).

#### Prediction of Rate Reduction by PKA Inhibition

Recent experimental studies discovered that emergence of spontaneous  $Ca^{2+}$  releases (i.e.,  $Ca^{2+}$  clock ticking) in rabbit SANC is driven by a relatively high PKA activity in the basal state (67). More specifically, critical experimental evidence for this basal clock mechanism and its importance for both basal AP firing and rate regulation was obtained by using a PKA inhibitor PKI: grading basal PKA activity results in graded phospholamban dephosphorylation paralleled with graded rate decrease down to complete halt (67). In those experiments, a physiological-scale rate reduction by 22.6% was achieved by a moderate PKA inhibition with 1.7  $\mu$ M PKI, and we tested whether our model can reproduce this important result.

The function of the SR  $Ca^{2+}$  pump and its regulatory protein phospholamban are mimicked by  $P_{up}$  variations in our model. Accordingly, PKI effect can be interpreted and tested in terms of  $P_{up}$  decrease. Since  $P_{up}$  broadly modulates the AP firing rate (Fig. 9A), a  $P_{up}$  reduction from 12 to 5.1 mM/s (vector bf in Fig. 10A) is sufficient to explain the 22.6% rate reduction. However, this  $P_{up}$  reduction by 57.5% is more than one might expect from the half-maximum effect of phospholamban de-

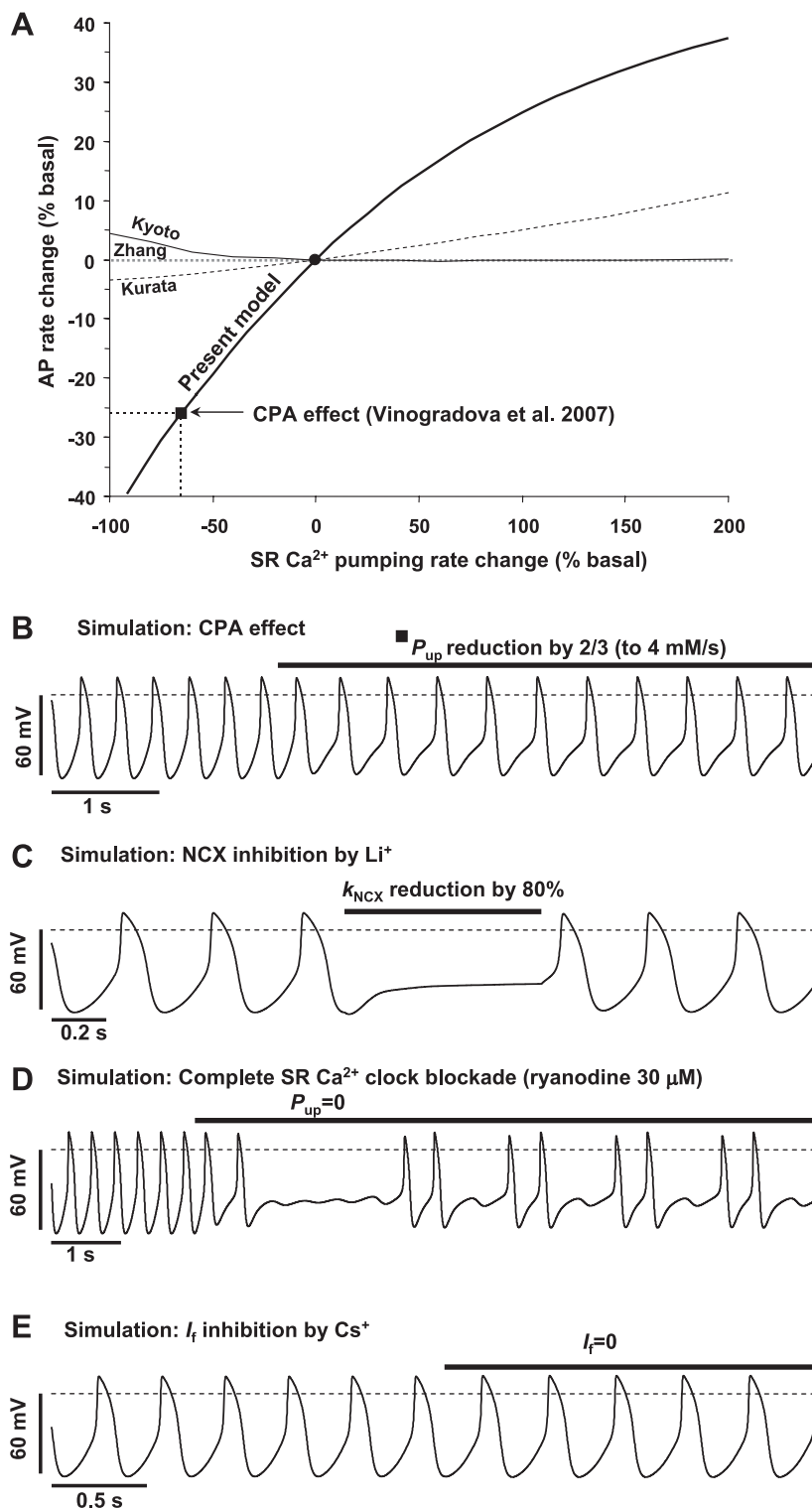


Fig. 9. Predictions of chronotropic perturbations by our basal AP firing model. A: finding the system solution (Present model, black box) for the rate reduction produced experimentally by a specific SR Ca<sup>2+</sup> pump inhibition with cyclopiazonic acid (CPA) (66). Also shown: predictions of small (if any) rate modulation produced by changes in the Ca<sup>2+</sup> SR pumping rate in Kyoto model (Ref. 57; “Kyoto”), Zhang et al. (73) model (“Zhang”), and Kurata model. B–E: predictions of our basal model for voltage ( $V_m$ ) dynamics, with instant model parameter changes (black bars) simulating various chronotropic interventions indicated by respective labels in the panels.  $k_{NCX}$ , scaling factor for  $I_{NCX}$ .

phosphorylation found somewhere between 1.7 and 5 μM PKI (67), pointing to a possible contribution of other mechanism(s).

Could it be sarcolemmal ion channels? In fact,  $I_f$  is modulated directly by cAMP (12) but not by PKA.  $I_{Kr}$  is not modulated by PKA but rather PKC (14); but slow component of the delayed rectifier K<sup>+</sup> current ( $I_{Ks}$ ), which is modulated by PKA (62), has a negligible basal density in rabbit SANC. The most plausible candidate is  $I_{CaL}$ , but experimental results on  $I_{CaL}$  modulation by

PKA inhibition and/or by acetylcholine in SANC greatly vary from extremely strong inhibition by 85% (52) to no effect in at least two studies (19, 50). The difference in results can be due at least in part to technical difficulties to measure and to interpret  $I_{CaL}$  inhibition when the current undergoes substantial rundown in whole cell patch clamp (e.g., >50% during 5 min in Ref. 52).

Thus we tested the effect of a rather small inhibition of basal  $g_{CaL}$  such as 15.5% [half-maximum  $I_{CaL}$  inhibition reported by

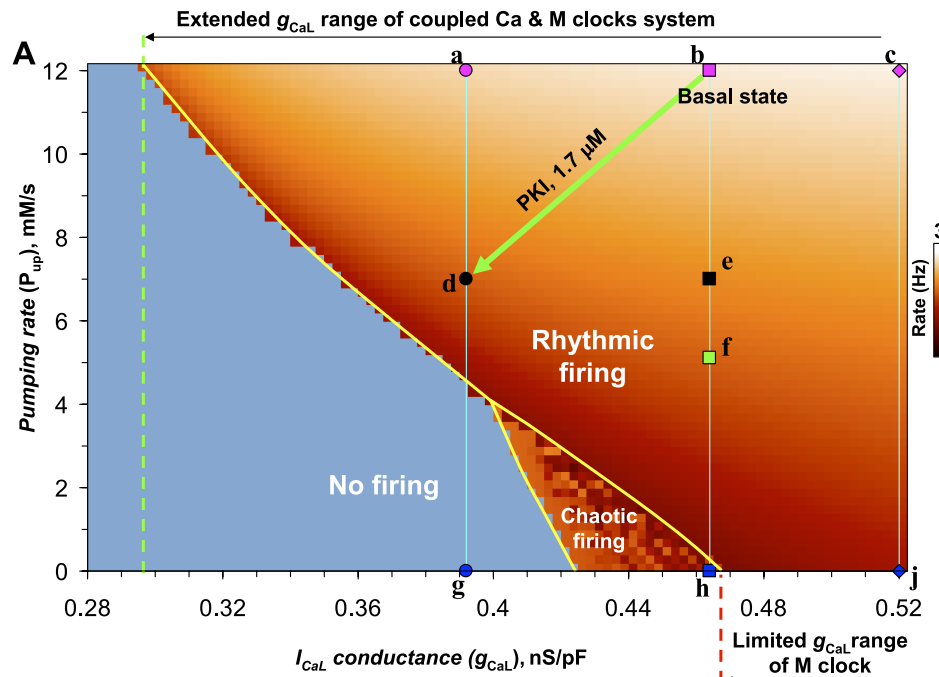
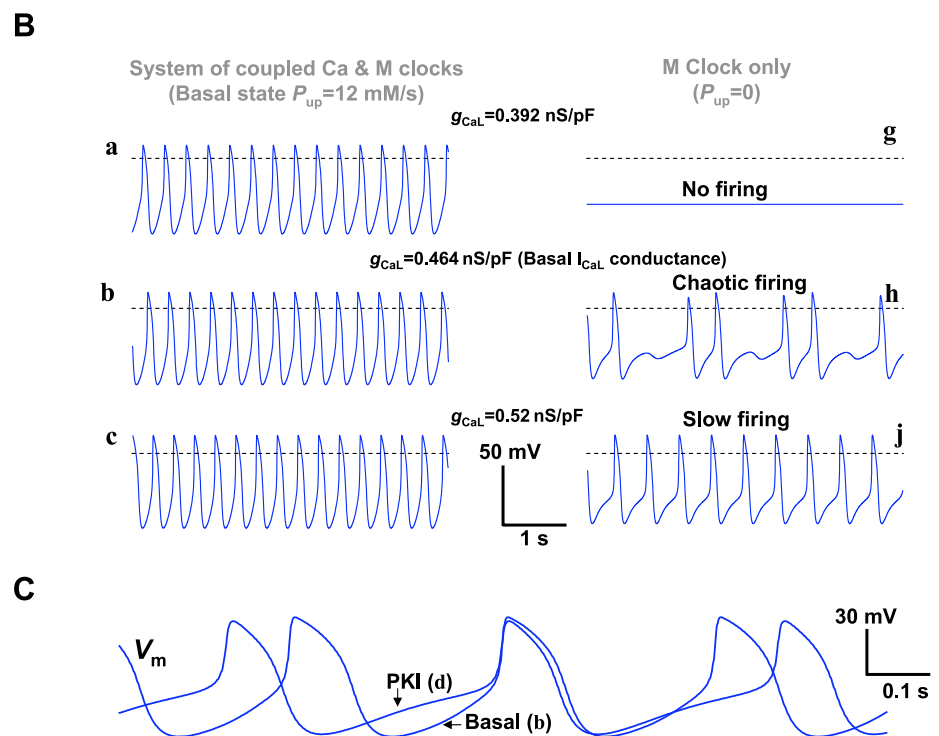


Fig. 10.  $\text{Ca}^{2+}$  clock confers the system robustness. *A*: our parametric system analysis with simultaneous variations in  $I_{\text{CaL}}$  conductance and SR  $\text{Ca}^{2+}$  pumping rate. The image shows the result of  $97 (x) \times 61 (y) = 5,917$  simulations (each pixel =  $0.0025 \text{ nS/pF} \times 0.2 \text{ mM/s}$ ). The resultant AP firing rate of the system is illustrated by graded color coded by the color map on the right; areas of no firing and chaotic firing are also marked and separated by yellow line. *B*: simulation traces for specific points of interest in *A*, illustrating more robust system operation when  $\text{Ca}^{2+}$  clock is functional. *C*: simulations of the effect of moderate PKA inhibition by  $1.7 \mu\text{M}$  PKI (represented by vector *bd* in *A*). M clock, membrane clock.



Zaza et al. (72)]. In practice, such small current changes are difficult to detect by patch-clamp technique because of registration noise and aforementioned  $I_{\text{CaL}}$  rundown. Surprisingly, with this small  $g_{\text{CaL}}$  change, the 22.6% rate reduction can be achieved in the model with a much smaller, 41.6%  $P_{\text{up}}$  decrease (Fig. 10A, vector *bd* vs. *bf*; simulation traces in Fig. 10C). Since the effect of  $g_{\text{CaL}}$  reduction per se is very small (only 2.8%, vector *ba* in Fig. 10A),  $g_{\text{CaL}}$  and  $P_{\text{up}}$  changes exhibit a noticeable synergism in their rate slowing. This result of the smaller  $P_{\text{up}}$  reduction combined with the small  $g_{\text{CaL}}$  reduction (rather than of the large  $P_{\text{up}}$

reduction alone) is in a better agreement with experimental result in rabbit SANC that the half-maximum effect of phospholamban dephosphorylation is reached between 1.7 and  $5 \mu\text{M}$  PKI (67).

*Extreme Rate Acceleration by PKA Activation with cAMP (Phosphodiesterase Inhibition)*

We also tested whether our new model predicts important recent experimental results of extreme rate acceleration by phosphodiesterase inhibition, specifically a  $\sim 47\%$  rate in-

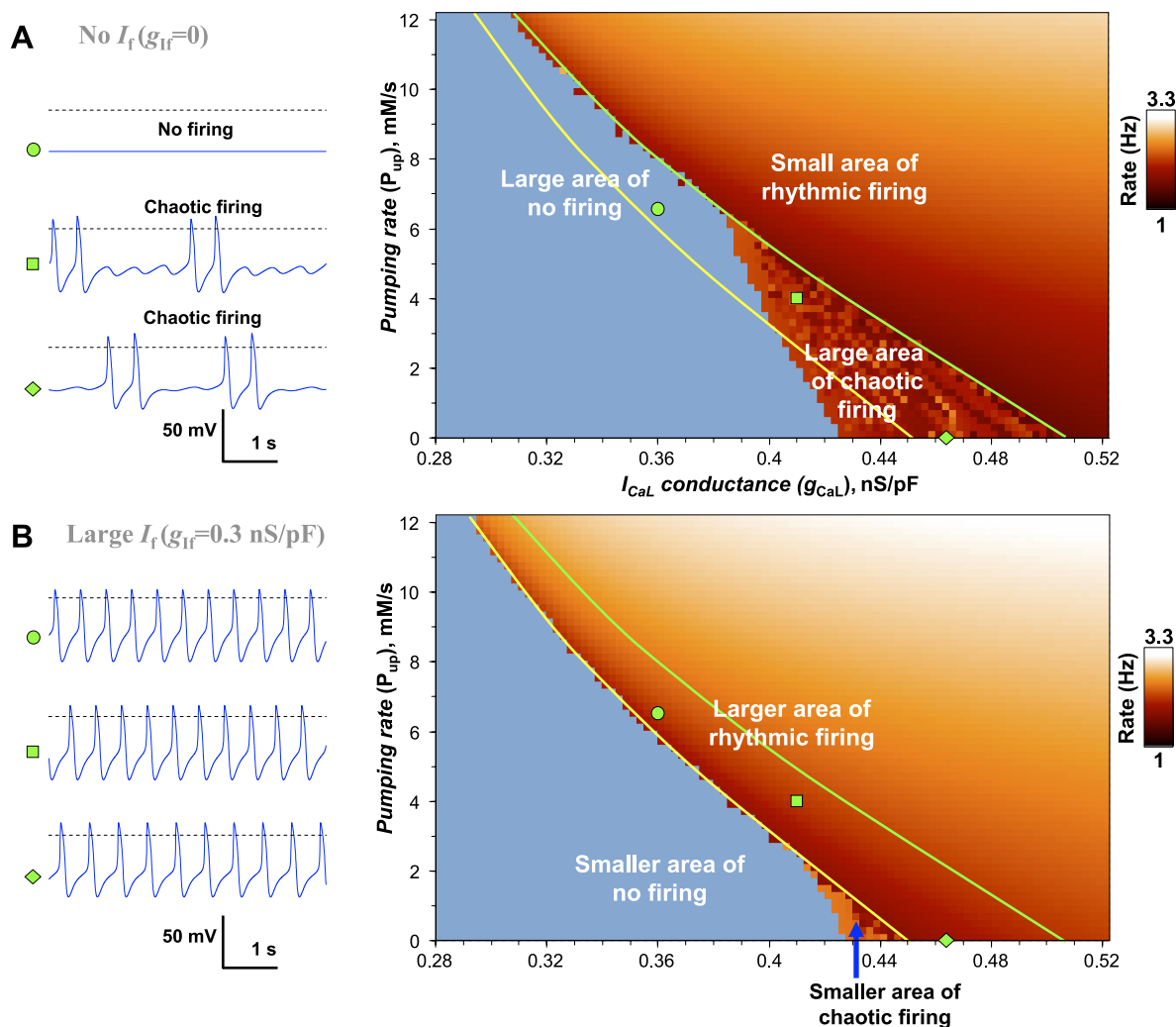


Fig. 11.  $I_f$  increases the system robustness at low AP rates. Our parametric system analysis with simultaneous variations in  $I_{CaL}$  conductance and SR  $Ca^{2+}$  pumping rate was performed at 2 extreme settings: no  $I_f$  (A) and large  $I_f$  (B). The system featuring  $I_f$  has smaller areas of no firing and chaotic AP firing. The results are illustrated by images, with the size (5,917 simulations) and the pixel size ( $0.0025$  nS/pF  $\times$   $0.2$  mM/s) being identical to those in Fig. 10A. Simulations for some specific points of interest within the explored parametric space are depicted on the left.  $g_{If}$ ,  $I_f$  conductance.

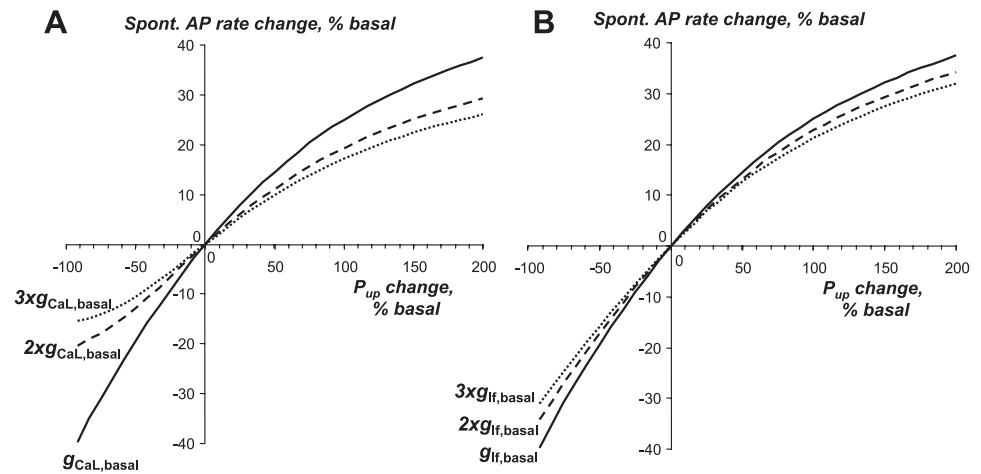
crease by phosphodiesterase 3 inhibitor milrinone in rabbit SANC (68). It was shown that this effect is linked to dramatic (9-fold) increase of basal cAMP resulting in strong PKA activation. We introduced changes for ion currents that were reported under these conditions:  $g_{CaL}$  increased by 45%;  $I_{Kr}$  increased by 12%, and its activation was shifted by 5 mV toward negative potentials (68); and a saturation shift of  $I_f$  activation curve by cAMP to its half-maximum activation voltage ( $V_{f,1/2}$ ) of  $-58.06$  mV, predicted by Eq. 7 in Demir et al. (9) model, was also included.

Although the uptake rate  $P_{up}$  could not be directly measured experimentally in SANC, both cAMP and phospholamban phosphorylation were found to be dramatically increased by milrinone (68). Therefore, in addition to ion current changes noted above, we also gradually increased  $P_{up}$  ("Ca & M clocks" curve in Fig. 13A) in attempt to find the system parametric solution for this extreme case. Indeed, the system yielded a unique solution for the 47% rate increase when  $P_{up}$  was increased  $\sim 4$ -fold (from 12 to 46 mM/s; black square in Fig. 13A). The system solution was also found at a slightly

higher  $P_{up}$  of 55 mM/s, when membrane clock was not changed ("Ca clock only," black circle in Fig. 13A).

In contrast, when  $Ca^{2+}$  clock was not changed, membrane clock has a limited range of rate modulation: the aforementioned changes of membrane clock alone increased the AP firing rate by only 12.8% (black diamond in Fig. 13A), in line with experimental results that demonstrate the major role of  $Ca^{2+}$  clock in the SANC rate acceleration by phosphodiesterase inhibition (68). In contrast to precisely timed AP ignitions by  $Ca^{2+}$  clock, ion channels modulate AP rate via a complex interplay of their effects on both DD and AP durations. This leads to a paradoxical behavior of some classic models lacking  $Ca^{2+}$  clock: these models decrease their AP firing rate when  $I_{CaL}$  increases, i.e., opposite to experimental results in cardiac pacemaker cells (55). For example, aforementioned  $g_{CaL}$  increase by 45% produces a 3% rate decrease in the Kurata model, as the AP duration increase prevails (data not shown). Despite a prominent increase in the action potential duration at 50% repolarization ( $APD_{50}$ ; from 101 to 113.4 ms), our basal firing model predicts a 3% rate increase in this instance. Thus

Fig. 12. The range of regulation of spontaneous (Spont.) AP firing rate by  $P_{up}$  substantially shrinks as  $g_{CaL}$  (A) or  $g_{If}$  (B) increases. The curves illustrate the results of our model sensitivity analysis (basal model) for spontaneous AP rate change, with  $P_{up}$  varying from its basal value of 12 mM/s. The respective conductance values are shown at the curves, with 2× or 3× representing their multiples.



our model overcomes the paradox of some classic models because in addition to its direct electrogenic contribution, increased  $I_{CaL}$  shortens DD by acting as a part of the system  $Ca^{2+}$  clock (Fig. 1). As to  $I_f$ , it does not affect AP duration, but its activation shift alone (to  $V_{f,1/2} = -58.06$  mV) produces only a minor rate increase in our basal model or Kurata model: 2.9 or 4.1%, i.e., when  $Ca^{2+}$  clock is unchanged or lacking, respectively.

We performed additional model simulations to further explore the mechanism of the milrinone effect (Fig. 13B). Interestingly, our model predicts notable decrease in diastolic  $I_f$  despite its activation shift and a much faster rate of rise. This diastolic  $I_f$  amplitude decrease occurs because of insufficient time for  $I_f$  to activate at this extremely high AP firing rate and short DD. In contrast, diastolic  $j_{SRcarel}$  amplitude approximately tripled, and the respective diastolic  $I_{NCX}$  more than doubled ( $17.7 \rightarrow 47.3$  pA or  $0.55 \rightarrow 1.48$  pA/pF). This model prediction is very close to the experimental estimate of the  $I_{NCX}$  increase from 0.7 to 1.5 pA/pF measured in rabbit SANC under similar conditions (68). We also compared simulations of cytosolic  $Ca^{2+}$  ( $Ca_i$ ) transient kinetics in control and with strong cAMP increase produced by milrinone (Fig. 13B, bottom). Milrinone shortened duration of the simulated AP-induced  $Ca^{2+}$  transients (from AP upstroke to 90% transient decay) by  $\sim 20\%$ , i.e., close to  $\sim 25\%$  measured experimentally in rabbit SANC under these conditions (68). Thus our model and experimental data validate each other to indicate that  $P_{up}$  likely substantially increases in SANC when intracellular cAMP surges.

It is important to note, again, that the model predictions shown in Fig. 13 are the unique property of the present model. Previous SANC models have very small sensitivity (if any) to variations in SR pumping rate (Fig. 9A) and, therefore, do not provide solutions either for rate slowing with CPA or for the extreme rate acceleration by phosphodiesterase inhibition.

## DISCUSSION

We developed a novel unique numerical model of normal cardiac cell pacemaker function, which is based on classic formulations of SR and membrane function. The model requires a single, straight-forward assumption: the existence of submembrane  $Ca^{2+}$  clock in SANC, an assumption based on

solid experimental evidence of the emergence and critical functional importance of spontaneous rhythmic subsarcolemmal releases in rabbit SANC under normal physiological conditions [original studies (4, 5, 37, 38, 42, 65, 67, 68, 70), editorials (2, 7, 34, 40), and recent reviews (31, 32, 41, 43, 45)]. By varying rates of SR  $Ca^{2+}$  pumping and release, we determined the parametric space of the oscillatory SR behavior and then explored how this modeled  $Ca^{2+}$  oscillator integrates with classic membrane voltage oscillator of SANC to insure robust and flexible spontaneous AP firing.

The concept of interacting oscillators has been also previously proposed as a potential mechanism of entrainment of individual SANC within sinoatrial node (22) and to pathological rhythms under  $Ca^{2+}$  overload conditions (63) or formed by more than single pacemaker area ("ectopic" pacemakers; Ref. 1) or by uncoupling of  $Ca^{2+}$  cycling and excitation waves within myocardium (54).

### The Coupled Oscillators Model Validates Recent Experimental Results

Surprisingly, our numerical system of coupled oscillators reproduced basically all recently discovered new behavioral details of cardiac cell pacemaker function (listed below), none of which can be predicted by existing numerical SANC models [including Zhang et al. (73) model, Kurata model, and Kyoto model; Fig. 9A] that do not incorporate the  $Ca^{2+}$  clock.

1. AP ignition involves cooperative action of both  $Ca^{2+}$  and membrane clock. The model predicts the occurrence of spontaneous submembrane releases ( $Ca^{2+}$  clock ticks) resulting in  $I_{NCX}$  activation (ignition currents) and late DD acceleration (Fig. 4, red arrows) as observed experimentally in rabbit SANC (4, 5, 42). A recent morphological study of SANC showed that RyRs are indeed strongly expressed and colocalized with NCX (37). Thus, in both our model formulation and spontaneously firing SANC, RyR-NCX cross talk insures effective coupling of the rhythmic spontaneous  $Ca^{2+}$  signals of the synchronous RyR openings to the late DD acceleration that is sufficient to reach the AP threshold from the levels of the afterhyperpolarizations (Figs. 5D and 7E) produced by early and mid-DD mechanisms such as  $I_{Kr}$  inactivation and  $I_f$  activation. It is important to note that prediction of the timing of spontaneous  $Ca^{2+}$  release occurrence is a specific characteristic of the novel model; this timing could not be predicted by our prior

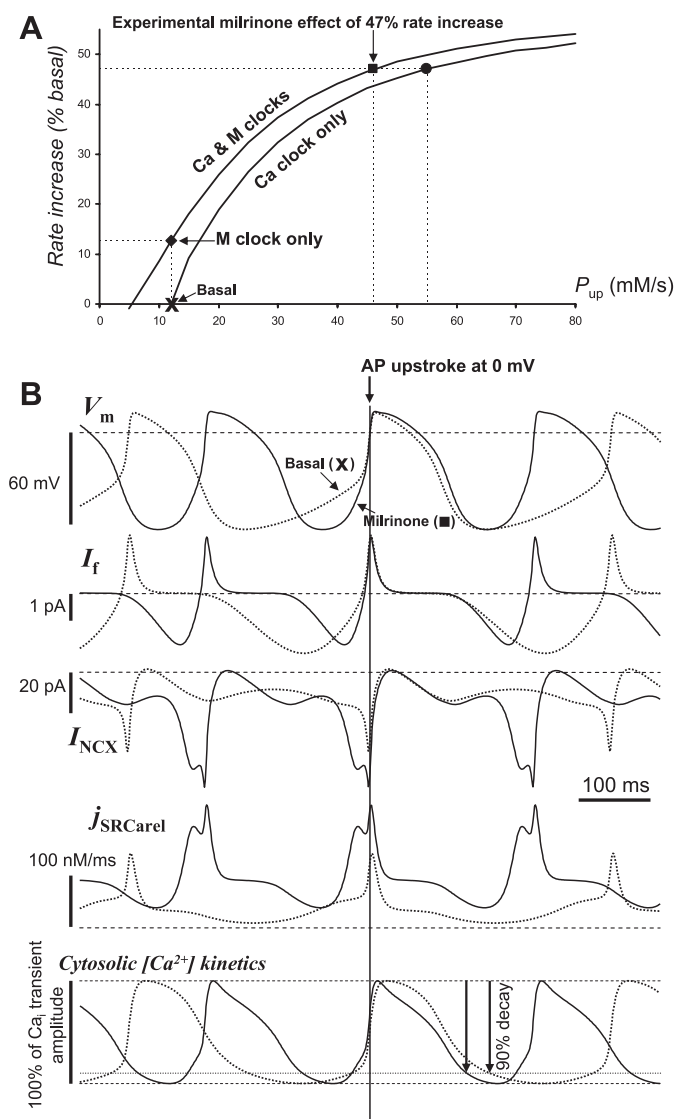


Fig. 13. Our model predicts extreme rate acceleration by PKA activation with cAMP increase (upon phosphodiesterase 3 inhibition with milrinone). *A*: finding system solution for the reported milrinone effect (47% basal rate increase) when membrane clock ( $I_{CaL}$ ,  $I_f$  and  $I_{Kr}$ ) was changed according previously reported experimental data (68) and  $P_{up}$  was graded ("Ca & M clocks," black box) or when only  $P_{up}$  was graded ("Ca clock only," black circle) from basal state firing ("Basal"). Model predicts 12.8% rate increase when only membrane clock was changed ("M clock only"). *B*: simulations illustrating the mechanism of the milrinone effect. Compared are simulated traces of  $V_m$ ,  $I_f$ ,  $I_{NCX}$ ,  $j_{SRCarel}$ , and  $Ca_i$  kinetics for basal state AP firing ("Basal," dotted lines) vs. respective traces for the milrinone effect ("Milrinone," solid lines), which is depicted by black box in the plot in *A*.

model of  $Ca^{2+}$  diastolic release driven by a simple sinusoidal function (42).

2. *High level of PKA activity and phospholamban phosphorylation in the basal state in rabbit SANc* (67). In our model,  $P_{up}$  variations mimic the function of the SR  $Ca^{2+}$  pump and its regulatory protein phospholamban. Accordingly, the high level phospholamban phosphorylation is described well by our model because  $P_{up}$  solution for the 3-Hz basal rate was found in the middle of the  $P_{up}$ -rate modulation curve (Fig. 9A).

3. *The enhanced system flexibility via  $Ca^{2+}$  clock modulation confers the novel pacemaker rate regulation mechanism.* The high level of PKA activity in the basal state insures basal  $Ca^{2+}$  clock ticking. Therefore, grading PKA activity up and down (e.g., via  $\beta$ -ARs and m-AChRs) varies the  $Ca^{2+}$  clock ticking speed up and down, resulting in broad rate regulation in rabbit SANc (Refs. 67 and 38, respectively). Although the present study does not specifically address the complex interplay of  $Ca^{2+}$  and membrane clocks in autonomic regulation of cardiac pacemaker function, our novel model strongly supports this new PKA-dependent (phospholamban phosphorylation) rate regulation mechanism: decelerating or accelerating  $Ca^{2+}$  clock ticking by grading  $P_{up}$  modulates the pacemaker rate within an extremely broad range from  $-40$  to  $+53\%$  from a basal rate of 3 Hz, respectively (Figs. 9A and 13A).

It is important to note, however, that the full-scale rate increase of  $+53\%$  cannot be probably explained by the  $P_{up}$  modulation solely by the phospholamban phosphorylation mechanism. Indeed, such rate boost requires a  $P_{up}$  increase of up to  $\sim 4$ -fold (Fig. 13A), whereas the  $P_{up}$  modulation via phospholamban phosphorylation is limited only to 2–3 times [depending on cytosolic  $Ca^{2+}$  (8)]. This indicates that, to reach the extreme rate acceleration, phospholamban/PKA signaling is likely further amplified and/or complemented by some additional factors, such as cell  $Ca^{2+}$  per se and CaMKII signaling (Fig. 5A). On the other hand, a physiological rate regulation range of  $\pm 20\%$  of basal beating rate can be easily achieved in the model with physiologically reasonable (i.e., moderate)  $P_{up}$  changes via phospholamban/PKA signaling (either alone or better together with respective moderate ion channel changes). Indeed, a 22.6% rate reduction is achieved with a 41.6% of  $P_{up}$  decrease (vector bd in Fig. 10A); but  $+20\%$  is achieved with a  $\sim 33\%$  or  $\sim 75\%$   $P_{up}$  increase (Fig. 13A, "Ca & M clocks" or "Ca clock only," respectively). We also want to note that the hypothetical physiological rate regulation by  $P_{up}$  is very effective in our model within the above mentioned moderate range but become saturated (i.e., ineffective) at higher  $P_{up}$  values (Fig. 13A).

4. *Major rate and rhythm disturbances on  $Ca^{2+}$  clock obstruction.* These included effects of SR  $Ca^{2+}$  pump inhibition with CPA (Fig. 9B), NCX inhibition by acute extracellular  $Na^+$  replacement by  $Li^+$  (Fig. 9C), ineffective RyR function with ryanodine (Fig. 9D), and inhibition of PKA-dependent phosphorylation with PKI (Fig. 10C, vector bd in Fig. 10A).

#### Additional Novel Model Insights

Our new model not only validates recent experimental findings, but also provides novel mechanistic insights into cardiac pacemaker function, which can be neither logically deduced from the existing experimental data nor predicted by previous numerical modeling of SANc:

1. *The first model of a physiological  $Ca^{2+}$  clock.* As mentioned in the Introduction, a contemplative mechanism of cardiac  $Ca^{2+}$  clock as cycles of  $Ca^{2+}$  uptake and release by the SR had been suggested as early as in 1979 by Tsien et al. (63). However, spontaneous  $Ca^{2+}$  oscillations in cardiac cells are traditionally associated with pathological conditions (61), i.e., specifically with high intracellular  $Na^+$  leading to  $Ca^{2+}$  overload (47). The novel and original finding of our study is that the physiological  $Ca^{2+}$  clock is not limited to the SR  $Ca^{2+}$  clock

but also includes balanced sarcolemmal  $\text{Ca}^{2+}$  fluxes of  $I_{\text{CaL}}$  and NCX (Fig. 1, bold arrows) that substantially enhance the  $\text{Ca}^{2+}$  clock performance. The coupled physiological  $\text{Ca}^{2+}$  clock exhibits the robust functional paradigm “the faster, the stronger” (Fig. 6B, inset), whereas the isolated SR  $\text{Ca}^{2+}$  clock cannot sustain high-amplitude oscillations at higher rates, i.e., “the faster, the weaker” (Fig. 3). Our coupled  $\text{Ca}^{2+}$  clock operates at a physiological intracellular  $\text{Na}^+$  (10 mM) and physiological cell  $\text{Ca}^{2+}$  loads (reported by  $C_{\text{nSR}}$  levels). A reasonable range of basal AP firing rates from 2.56 to 3 Hz is achieved in our model with physiological  $C_{\text{nSR}}$  levels from 1 to 1.5 mM (Fig. 7), which were reported for rabbit cardiac cells (58). At higher rates, the  $\text{Ca}^{2+}$  load in our model increases (Fig. 7A), also in a good agreement with experimental results of larger caffeine-induced transients at higher AP firing rates, e.g., on  $\beta$ -AR stimulation (70) or phosphodiesterase inhibition (68).

In contrast to Shannon model of one compartment SR (i.e.,  $C_{\text{nSR}} = C_{\text{tSR}}$ ) of ventricular myocytes (59), an important characteristic of two-compartment SR function in our model is that the amplitude of  $C_{\text{nSR}}$  oscillations remains small compared with  $C_{\text{nSR}}$  average level (Fig. 7A). This allows maintenance of a substantial  $\text{Ca}^{2+}$  reserve in the system (in other words, the system keeps some fuel reserve in its “fuel tank”); recapitulating an experimental observation of strong caffeine-induced  $\text{Ca}^{2+}$  transients at any oscillation cycle phase in rabbit SANC (70). Our model simulations indicate that this might be important for robust pacemaker function: when  $\text{Ca}^{2+}$  pump is blocked (Fig. 9D), this  $\text{Ca}^{2+}$  reserve insures generation of additional/reserved AP ignitions before SR gets empty and system fails. Future biophysical measurements in SANC are required to clarify importance of this cell  $\text{Ca}^{2+}$  reserve as well as specific contributions of inter-SR diffusion,  $P_{\text{up}}$ , RyR restitution,  $\text{Ca}^{2+}$  channels, and NCX to the  $\text{Ca}^{2+}$  clock amplitude and ticking speed.

2. *The fine structure of the SR  $\text{Ca}^{2+}$  release in SANC has three distinct phases (Fig. 4, red trace in bottom).* Our recent pilot study using a high-speed camera in rabbit SANC (51) has demonstrated  $\text{Ca}^{2+}$  sparks as initial form of  $\text{Ca}^{2+}$  release during DD, followed by propagating release before the AP-initiated  $\text{Ca}^{2+}$  transient.

3. *Mechanisms of arrhythmic AP firing in the system are associated with uncoupling of  $\text{Ca}^{2+}$  and membrane clocks or uncoupling of components of membrane clock (e.g.,  $I_{\text{CaL}}$  and  $I_f$ ; Figs. 10 and 11, areas of “Chaotic firing”).* Our model predictions added  $I_f$  importance for the system performance when its firing rate decreases (Fig. 11), in line with recent surprising findings in HCN4 ( $I_f$  channel) knockout mice (15). It also supports an earlier concept first proposed by Noble et al. (48), i.e.,  $I_f$  has more time to activate within longer cycle lengths and thus acts as a “stabilizer” of the pacemaker rate. As intrinsic cycle length is substantially longer in atrioventricular node vs. that in sinoatrial node, this concept also explains a substantially stronger effect of  $I_f$  blockade in the atrioventricular node (35).

4.  *$\text{Ca}^{2+}$  clock confers robustness to the SANC pacemaker system.* For the first time, we described  $\text{Ca}^{2+}$  clock as a new critical dimension in robust initiation of cardiac impulse. Our broad parametric analysis demonstrates that any enhancement of either mechanism ( $P_{\text{up}}$ ,  $I_{\text{CaL}}$ , or  $I_f$ ) broadens the fail-safe ranges for the other two mechanisms (Figs. 10 and 11). The

robust operation of the SANC pacemaker system is insured by tight cooperation of  $\text{Ca}^{2+}$  and membrane clocks as they commit their moderate combined resources for SANC basal firing (Fig. 10A, “Basal state”), preserving substantial reserve to effectively handle extreme perturbations. In our example of simulation of an extreme rate increase produced by phosphodiesterase inhibition (Fig. 13), the preserved reserve of  $\text{Ca}^{2+}$  clock (i.e., reserve in  $P_{\text{up}}$  rate modulation) is required and sufficient to effect a remarkable, 53% AP rate increase. Under these conditions, intracellular cAMP raises by ninefold (68) and supposedly saturates an  $I_f$  activation voltage shift and thereby increases  $I_f$  rate of rise; however, the diastolic  $I_f$  amplitude still decreases because of insufficient time for activation during shorter DD duration (Fig. 13B,  $I_f$ ). Thus reserve recourses of membrane clock alone (when  $\text{Ca}^{2+}$  clock parameters are fixed in our model) insure rate increases of only up to 12.8% (black diamond in Fig. 13A), i.e., insufficient to reach such higher (+53%) rates.

#### *About Balance of Robustness and Flexibility in the Present and Prior SANC Models*

We interpreted the results of our simulations in the section *High  $I_{\text{CaL}}$  and  $I_f$  Conductances Limit Pacemaker Flexibility* (Figs. 10–12) to indicate that the system of coupled clocks with moderate (i.e., physiologically reasonable) values of  $g_{\text{CaL}}$  and  $g_{\text{If}}$  likely achieves the highest possible balance of robustness and flexibility of SANC function. However, a high balance of robustness and flexibility has been also achieved in some previous, essentially membrane-delimited models. For example, Demir et al. (9) model also exhibits robust AP firing and simultaneously reproduces full-scale rate regulation via m-AChRs and  $\beta$ -ARs. However, the Demir et al. model was based on its earlier (1994) basal AP firing model version (10) that incorporated the knowledge about SANC electrophysiology at that time. That older model included a relatively large voltage-gated sodium ( $I_{\text{Na}}$ ) conductance and  $I_{\text{CaT}}$  conductance, which, according to more recent data, are absent or much less in primary rabbit SANC, respectively (44, 71). Both  $I_{\text{Na}}$  and  $I_{\text{CaT}}$  have low voltage activation thresholds and, therefore, strongly amplified the initial cAMP-sensitive signaling of  $I_f$ -induced early depolarization in the Demir et al. (9) model. Another, more recent pacemaker regulation mechanism is via a sustained, nonselective, inward current  $I_{\text{st}}$  in the Kyoto model of guinea pig SANC (16, 57). However, as we noted earlier, molecular origin and specific blockers for  $I_{\text{st}}$  have not yet been identified;  $I_{\text{st}}$  exhibits many properties of  $I_{\text{CaL}}$  and  $I_{\text{NCX}}$  and, therefore, might not even be a discrete entity. Thus the difference in the models is in their late DD mechanisms, which are: “LCR-induced  $I_{\text{NCX}} + I_{\text{CaL}}$ ” in the present model; “ $I_{\text{Na}} + I_{\text{CaT}} + I_{\text{CaL}}$ ” in the Demir et al. (9) model; and “ $I_{\text{st}} + I_{\text{CaL}}$ ” in the Kyoto model (16, 57). If we exclude  $I_{\text{Na}}$ ,  $I_{\text{CaT}}$ , and  $I_{\text{st}}$  as major regulation players in primary SANC, then the regulation only via  $I_f$  and/or  $I_{\text{CaL}}$  seems to be insufficient to explain the high balance of robustness and flexibility of SANC function (40) so that our LCR-induced  $I_{\text{NCX}}$  mechanism may be suggested as the missing link in the mystery of cardiac automaticity (see recent review in Ref. 32). A minor role of  $I_f$  in pacemaker rate regulation has been also demonstrated by recent functional genetics studies with  $I_f$  knockout (15).

### Model Limitations

Our presentation is limited by the scope of a research paper as well as by the specific aim to develop and to initially explore the first prototype SANC model of dynamically interacting  $\text{Ca}^{2+}$  and membrane clocks and having minimum changes in classic formulations. Thus, although it is extremely tempting for us to further evaluate the importance of various parameters for behavior of the new modeled system, we limited our analysis to only a few key parameters. Since many model parameters have ascended from prior models of ventricular and atrial myocytes, our SANC-specific formulations for the coupled  $\text{Ca}^{2+}$  and membrane clocks will require further development and tuning as new experimental data in SANC emerge.

An important future model development is related to SR geometry under sarcolemma that ultimately determines the fine spatiotemporal structure of the  $\text{Ca}^{2+}$  release in SANC that could not be approximated here. In fact, the released  $\text{Ca}^{2+}$  in our model is instantly diluted in a relatively large subspace volume that was originally defined in Kurata model as a 20-nm space below the entire sarcolemma. This explains, in part, why SR  $\text{Ca}^{2+}$  oscillations require a substantial increase in the release rate constant  $k_s$  compared with that in Shannon model of ventricular cell SR operating as an ensemble of  $\text{Ca}^{2+}$  release units (CRUs).

Actually, RyRs seem to be arranged in clusters under sarcolemma in SANC (Fig. 2 in Ref. 37) and thus probably form subsarcolemmal CRUs (SANC lack T-tubules). In this instance, RyRs release  $\text{Ca}^{2+}$  into a relatively small volume of cleft space where individual jSRs of CRUs approach sarcolemma. Our pilot experimental study of 2-D  $\text{Ca}^{2+}$  signals showed that wavelet-like LCRs in SANC are indeed formed by the stochastic  $\text{Ca}^{2+}$  sparks propagating in a “fire-diffuse-fire” manner under sarcolemma (51). One recent numerical realization of such advanced  $\text{Ca}^{2+}$  release mechanism in SANC includes local  $\text{Ca}^{2+}$  diffusion and propagating CICR within dynamic corridors of refractoriness for the CRUs under sarcolemma (39). Thus future modeling of SANC function will probably include a stochastic mechanism of LCR generation by CRUs. It merits emphasis, however, that results of such detailed modeling will not necessarily contradict to the results of the present study. Indeed, experimental studies showed that it is the lumped signal of synchronized LCRs, well-approximated in the present model by variable  $j_{\text{SRcarel}}$ , that drives both basal AP firing and the AP rate modulation of SANC (38, 42, 65, 67).

Another potentially important model limitation is that we fixed intracellular  $\text{Na}^+$  concentration; modeling of  $\text{Na}^+$  dynamics was not a specific aim of our study and requires further special consideration.

### Summary

The pacemaker of the heart generates billions of uninterrupted beats at greatly varying rates during the life span and therefore must be an extremely robust and simultaneously flexible system. A rather simple numerical release-pumping-delay SR  $\text{Ca}^{2+}$  clock described here (Figs. 1–3) possesses an extreme flexibility (1.3–6.1 Hz), but its robustness is limited, as it cannot sustain high-amplitude oscillations at high rates in the absence of interactions with membrane clock. The SANC

pacemaker system of the two coupled oscillators keeps the advantage of the superior flexibility of the SR  $\text{Ca}^{2+}$  clock but simultaneously rebalances cell  $\text{Ca}^{2+}$  (via sarcolemmal  $\text{Ca}^{2+}$  fluxes of  $I_{\text{CaL}}$  and NCX; Figs. 1 and 7) to insure higher  $\text{Ca}^{2+}$  oscillation amplitudes at higher rates (Fig. 6B, *inset*, and Fig. 7). Operating in antiphase fashion,  $\text{Ca}^{2+}$  clock, in turn, evokes rhythmic APs by critically timed (short but sufficiently strong) NCX ignition currents (Fig. 5D) during late DD (Fig. 4, red arrow) when the prior AP is completing its recovery (i.e., afterhyperpolarization; Fig. 5D).

Robustness is a fundamental property of evolvable complex biological systems (23); a simple mechanism cannot handle extreme perturbations because it does not possess safety reserves. The heterogeneous redundancy of the oscillators (chemical  $\text{Ca}^{2+}$  clocks of the SR and electrical clocks of the surface membrane ion channels) allows basal state AP firing with moderate recourses of each clock in our numerical model of SANC pacemaker system, embracing smaller  $P_{\text{up}}$ ,  $I_{\text{CaL}}$ , and/or  $I_f$ , including those at which membrane clock, operating alone, fails (Figs. 10 and 11). This provides broad safety margins and confers extremely high robustness to the AP firing, including instances of extreme chronotropic perturbations (Fig. 13).

Thus our model offers a new integrative framework for conceptualizing SANC function and regulation as a robust and flexible system of the dynamically coupled  $\text{Ca}^{2+}$  and membrane oscillators. This new vision resolves existing apparent controversy of two extreme pacemaker concepts of cardiac automaticity driven by either oscillator alone (Refs. 25, 34; see also Ref. 18 vs. 30).

The present study also provides a theoretical basis for a novel general theory of regulation of heart contraction and rhythm (29, 43):  $\text{Ca}^{2+}$  cycling into and from SR by proteins common to both ventricular myocytes and pacemaker cells regulate the duty cycle of both cell types. Our simulations show that the Bowditch phenomenon known for ventricular myocytes as the faster, the stronger is also operational and critically important for pacemaker cells (29): whereas the stronger  $\text{Ca}^{2+}$  release at higher pacing rates results in stronger contractions of myocytes, the stronger diastolic  $\text{Ca}^{2+}$  release results in stronger accelerating DD in spontaneously firing SANC (Fig. 7). Thus  $\text{Ca}^{2+}$  releases directly regulate primary functions of these specialized cardiac cells resulting in stronger and more frequent heart beats, thereby comprising the effective regulation of blood pumping by the heart.

### Future Perspectives

Another level of complexity and robustness of cardiac pacemaker involves cell interactions within sinoatrial node. The late DD acceleration, in fact, is the earliest event within the central sinoatrial node pacemaker region (3) thus indicating that the LCR/NCX signals ignite spontaneous APs not only in isolated SANC, but also in the initiation site of the cardiac pacemaker tissue. Since SANC have copies of RyRs, NCX, and SERCA2 throughout the sinoatrial node, including those small-sized central cells (37), our model may be useful with respect to the development of new sinoatrial node tissue model to probe the role of the coupled  $\text{Ca}^{2+}$  cycling and membrane excitation to heart rate regulation (via PKA and CaMKII signaling) *in silico*, *vis-à-vis* multiple ambitious projects of

physiome, or in vivo by biological pacemakers. Targeting cellular dynamics instead of specific molecules offers a new opportunity to understanding and design of novel therapies to treat pacemaker abnormalities and arrhythmias (61).

#### ACKNOWLEDGMENTS

We thank Michael D. Stern for critical reading of the manuscript.

#### GRANTS

This research was supported by the Intramural Research Program of the National Institutes of Health, National Institute on Aging.

#### REFERENCES

1. Antzelevitch C, Jalife J, Moe GK. Electrotonic metabolism of pacemaker activity. Further biological and mathematical observations on the behavior of modulated parasystole. *Circulation* 66: 1225–1232, 1982.
2. Bers DM. The beat goes on: diastolic noise that just won't quit. *Circ Res* 99: 921–923, 2006.
3. Bleeker WK, Mackaay AJ, Masson-Pevet M, Bouman LN, Becker AE. Functional and morphological organization of the rabbit sinus node. *Circ Res* 46: 11–22, 1980.
4. Bogdanov KY, Maltsev VA, Vinogradova TM, Lyashkov AE, Spurgeon HA, Stern MD, Lakatta EG. Membrane potential fluctuations resulting from submembrane  $\text{Ca}^{2+}$  releases in rabbit sinoatrial nodal cells impart an exponential phase to the late diastolic depolarization that controls their chronotropic state. *Circ Res* 99: 979–987, 2006.
5. Bogdanov KY, Vinogradova TM, Lakatta EG. Sinoatrial nodal cell ryanodine receptor and  $\text{Na}^+$ - $\text{Ca}^{2+}$  exchanger: molecular partners in pacemaker regulation. *Circ Res* 88: 1254–1258, 2001.
6. Bozler E. Tonus changes in cardiac muscle and their significance for the initiation of impulses. *Am J Physiol* 139: 477–480, 1943.
7. Bridge JH, Davidson CJ, Savio-Galimberti E. A novel mechanism of pacemaker control that depends on high levels of cAMP and PKA-dependent phosphorylation: a precisely controlled biological clock. *Circ Res* 98: 437–439, 2006.
8. Colyer J, Wang JH. Dependence of cardiac sarcoplasmic reticulum calcium pump activity on the phosphorylation status of phospholamban. *J Biol Chem* 266: 17486–17493, 1991.
9. Demir SS, Clark JW, Giles WR. Parasympathetic modulation of sinoatrial node pacemaker activity in rabbit heart: a unifying model. *Am J Physiol Heart Circ Physiol* 276: H2221–H2244, 1999.
10. Demir SS, Clark JW, Murphey CR, Giles WR. A mathematical model of a rabbit sinoatrial node cell. *Am J Physiol Cell Physiol* 266: C832–C852, 1994.
11. DiFrancesco D. The contribution of the 'pacemaker' current ( $i_p$ ) to generation of spontaneous activity in rabbit sino-atrial node myocytes. *J Physiol* 434: 23–40, 1991.
12. DiFrancesco D, Tortora P. Direct activation of cardiac pacemaker channels by intracellular cyclic AMP. *Nature* 351: 145–147, 1991.
13. Guan S, Lu Q, Huang K. A discussion about the DiFrancesco-Noble model. *J Theor Biol* 189: 27–32, 1997.
14. Heath BM, Terrar DA. Protein kinase C enhances the rapidly activating delayed rectifier potassium current,  $I_{Kr}$ , through a reduction in C-type inactivation in guinea-pig ventricular myocytes. *J Physiol* 522: 391–402, 2000.
15. Herrmann S, Stieber J, Stockl G, Hofmann F, Ludwig A. HCN4 provides a 'depolarization reserve' and is not required for heart rate acceleration in mice. *EMBO J* 26: 4423–4432, 2007.
16. Himeno Y, Sarai N, Matsuoka S, Noma A. Ionic mechanisms underlying the positive chronotropy induced by beta1-adrenergic stimulation in guinea pig sinoatrial node cells: a simulation study. *J Physiol Sci* 58: 53–65, 2008.
17. Honjo H, Boyett MR, Kodama I, Toyama J. Correlation between electrical activity and the size of rabbit sino-atrial node cells. *J Physiol* 496: 795–808, 1996.
18. Honjo H, Inada S, Lancaster MK, Yamamoto M, Niwa R, Jones SA, Shibata N, Mitsui K, Horiuchi T, Kamiya K, Kodama I, Boyett MR. Sarcoplasmic reticulum  $\text{Ca}^{2+}$  release is not a dominating factor in sinoatrial node pacemaker activity. *Circ Res* 92: e41–e44, 2003.
19. Honjo H, Kodama I, Zang WJ, Boyett MR. Desensitization to acetylcholine in single sinoatrial node cells isolated from rabbit hearts. *Am J Physiol Heart Circ Physiol* 263: H1779–H1789, 1992.
20. Hund TJ, Kucera JP, Otani NF, Rudy Y. Ionic charge conservation and long-term steady state in the Luo-Rudy dynamic cell model. *Biophys J* 81: 3324–3331, 2001.
21. Huser J, Blatter LA, Lipsius SL. Intracellular  $\text{Ca}^{2+}$  release contributes to automaticity in cat atrial pacemaker cells. *J Physiol* 524: 415–422, 2000.
22. Jalife J. Mutual entrainment and electrical coupling as mechanisms for synchronous firing of rabbit sino-atrial pace-maker cells. *J Physiol* 356: 221–243, 1984.
23. Kitano H. Biological robustness. *Nat Rev Genet* 5: 826–837, 2004.
24. Kneller J, Ramirez RJ, Chartier D, Courtemanche M, Nattel S. Time-dependent transients in an ionically based mathematical model of the canine atrial action potential. *Am J Physiol Heart Circ Physiol* 282: H1437–H1451, 2002.
25. Kodama I, Honjo H, Boyett MR. Are we lost in the labyrinth of the sinoatrial node pacemaker mechanism? *J Cardiovasc Electrophysiol* 13: 1303–1305, 2002.
26. Krogh-Madsen T, Schaffer P, Skriver AD, Taylor LK, Pelzmann B, Koidl B, Guevara MR. An ionic model for rhythmic activity in small clusters of embryonic chick ventricular cells. *Am J Physiol Heart Circ Physiol* 289: H398–H413, 2005.
27. Kurata Y, Hisatome I, Imanishi S, Shibamoto T. Dynamical description of sinoatrial node pacemaking: improved mathematical model for primary pacemaker cell. *Am J Physiol Heart Circ Physiol* 283: H2074–H2101, 2002.
28. Kurata Y, Hisatome I, Imanishi S, Shibamoto T. Roles of L-type  $\text{Ca}^{2+}$  and delayed-rectifier  $\text{K}^+$  currents in sinoatrial node pacemaking: insights from stability and bifurcation analyses of a mathematical model. *Am J Physiol Heart Circ Physiol* 285: H2804–H2819, 2003.
29. Lakatta EG. Beyond Bowditch: the convergence of cardiac chronotropy and inotropy. *Cell Calcium* 35: 629–642, 2004.
30. Lakatta EG, Maltsev VA, Bogdanov KY, Stern MD, Vinogradova TM. Cyclic variation of intracellular calcium: a critical factor for cardiac pacemaker cell dominance. *Circ Res* 92: e45–e50, 2003.
31. Lakatta EG, Vinogradova T, Lyashkov A, Sirenko S, Zhu W, Ruknudin A, Maltsev VA. The integration of spontaneous intracellular  $\text{Ca}^{2+}$  cycling and surface membrane ion channel activation entrains normal automaticity in cells of the heart's pacemaker. *Ann N Y Acad Sci* 1080: 178–206, 2006.
32. Lakatta EG, Vinogradova TM, Maltsev VA. The missing link in the mystery of normal automaticity of cardiac pacemaker cells. *Ann N Y Acad Sci* 1123: 41–57, 2008.
33. Li Y, Sirenko SG, Vinogradova TM, Lyashkov AE, Zhu W, Juhaszova M, Ziman B, Wang S, Lakatta EG. High basal  $\text{Ca}^{2+}$ /calmodulin kinase II activity modulates spontaneous sarcoplasmic reticulum  $\text{Ca}^{2+}$  cycling that drives normal automaticity in sinoatrial nodal cells. *Circulation* 116: 86–87, 2007.
34. Lipsius SL, Bers DM. Cardiac pacemaking:  $I_f$  vs.  $\text{Ca}^{2+}$ , is it really that simple? *J Mol Cell Cardiol* 35: 891–893, 2003.
35. Liu J, Noble PJ, Xiao G, Abdelrahman M, Dobrzynski H, Boyett MR, Lei M, Noble D. Role of pacemaking current in cardiac nodes: insights from a comparative study of sinoatrial node and atrioventricular node. *Prog Biophys Mol Biol* 96: 294–304, 2008.
36. Luo CH, Rudy Y. A dynamic model of the cardiac ventricular action potential. I. Simulations of ionic currents and concentration changes. *Circ Res* 74: 1071–1096, 1994.
37. Lyashkov AE, Juhaszova M, Dobrzynski H, Vinogradova TM, Maltsev VA, Juhasz O, Spurgeon HA, Sollott SJ, Lakatta EG. Calcium cycling protein density and functional importance to automaticity of isolated sinoatrial nodal cells are independent of cell size. *Circ Res* 100: 1723–1731, 2007.
38. Lyashkov AE, Vinogradova TM, Younes A, Li Y, Nuss B, Spurgeon HA, Lakatta EG. Role of acetylcholine-activated potassium current ( $I_{K_{ACh}}$ ), hyperpolarization-activated current ( $I_f$ ), protein kinase A (PKA)-dependent phosphorylation and  $\text{Ca}^{2+}$  cycling in muscarinic receptor (M2R) regulation of spontaneous action potential rate (APR) in isolated rabbit sinoatrial node cells (SANC) (Abstract). *Biophys J Suppl*: 251, 2008.
39. Maltsev AV, Maltsev VA, Sirenko SG, Maltseva LA, Parsons SP, Lakatta EG, Stern MD. A simple stochastic mechanism of a roughly periodic  $\text{Ca}^{2+}$  clock within cardiac cells (Abstract). *Biophys J Suppl*: 344a, 2007.

40. Maltsev VA, Lakatta EG. Cardiac pacemaker cell failure with preserved  $I_f$ ,  $I_{CaL}$ , and  $I_{Kr}$ : a lesson about pacemaker function learned from ischemia-induced bradycardia. *J Mol Cell Cardiol* 42: 289–294, 2007.
41. Maltsev VA, Lakatta EG. Dynamic interactions of an intracellular  $Ca^{2+}$  clock and membrane ion channel clock underlie robust initiation and regulation of cardiac pacemaker function. *Cardiovasc Res* 77: 274–284, 2008.
42. Maltsev VA, Vinogradova TM, Bogdanov KY, Lakatta EG, Stern MD. Diastolic calcium release controls the beating rate of rabbit sinoatrial node cells: numerical modeling of the coupling process. *Biophys J* 86: 2596–2605, 2004.
43. Maltsev VA, Vinogradova TM, Lakatta EG. The emergence of a general theory of the initiation and strength of the heartbeat. *J Pharm Sci* 100: 338–369, 2006.
44. Mangoni ME, Fontanaud P, Noble PJ, Noble D, Benkemoun H, Nargeot J, Richard S. Facilitation of the L-type calcium current in rabbit sino-atrial cells: effect on cardiac automaticity. *Cardiovasc Res* 48: 375–392, 2000.
45. Mangoni ME, Nargeot J. Genesis and regulation of the heart automaticity. *Physiol Rev* 88: 919–982, 2008.
46. Noble D. Cardiac action and pacemaker potentials based on the Hodgkin-Huxley equations. *Nature* 188: 495–497, 1960.
47. Noble D. Modeling the heart—from genes to cells to the whole organ. *Science* 295: 1678–1682, 2002.
48. Noble D, Denyer JC, Brown HF, DiFrancesco D. Reciprocal role of the inward currents  $i_b$ ,  $i_a$  and  $i_f$  in controlling and stabilizing pacemaker frequency of rabbit sino-atrial node cells. *Proc Biol Sci* 250: 199–207, 1992.
49. Noble D, Noble SJ. A model of sino-atrial node electrical activity based on a modification of the DiFrancesco-Noble (1984) equations. *Proc R Soc Lond B Biol Sci* 222: 295–304, 1984.
50. Noma A, Trautwein W. Relaxation of the ACh-induced potassium current in the rabbit sinoatrial node cell. *Pflügers Arch* 377: 193–200, 1978.
51. Parsons SP, Vinogradova TM, Lyashkov AE, Spurgeon HA, Stern MD, Lakatta EG, Maltsev VA. Local  $Ca^{2+}$  waves rather than sparks boost the subplasmalemmal  $Ca^{2+}$  rise in late diastole of rabbit sinoatrial node cells: characterization in two dimensions (Abstract). *Biophys J Suppl*: 76a, 2007.
52. Petit-Jacques J, Bois P, Bescond J, Lenfant J. Mechanism of muscarinic control of the high-threshold calcium current in rabbit sino-atrial node myocytes. *Pflügers Arch* 423: 21–27, 1993.
53. Pikovski A, Rosenblum M, Kurths J. *Synchronization: A Universal Concept in Nonlinear Sciences*. New York: Cambridge Univ. Press, 2001.
54. Qu Z, Weiss JN. Dynamics and cardiac arrhythmias. *J Cardiovasc Electrophysiol* 17: 1042–1049, 2006.
55. Rubenstein DS, Lipsius SL. Mechanisms of automaticity in subsidiary pacemakers from cat right atrium. *Circ Res* 64: 648–657, 1989.
56. Sanders L, Rakovic S, Lowe M, Mattick PA, Terrar DA. Fundamental importance of  $Na^+$ - $Ca^{2+}$  exchange for the pacemaking mechanism in guinea-pig sino-atrial node. *J Physiol* 571: 639–649, 2006.
57. Sarai N, Matsuoka S, Kuratomi S, Ono K, Noma A. Role of individual ionic current systems in the SA node hypothesized by a model study. *Jpn J Physiol* 53: 125–134, 2003.
58. Shannon TR, Guo T, Bers DM.  $Ca^{2+}$  scraps: local depletions of free  $[Ca^{2+}]$  in cardiac sarcoplasmic reticulum during contractions leave substantial  $Ca^{2+}$  reserve. *Circ Res* 93: 40–45, 2003.
59. Shannon TR, Wang F, Puglisi J, Weber C, Bers DM. A mathematical treatment of integrated Ca dynamics within the ventricular myocyte. *Biophys J* 87: 3351–3371, 2004.
60. Stern MD, Song LS, Cheng H, Sham JS, Yang HT, Boheler KR, Rios E. Local control models of cardiac excitation-contraction coupling. A possible role for allosteric interactions between ryanodine receptors. *J Gen Physiol* 113: 469–489, 1999.
61. Ter Keurs HE, Boyden PA. Calcium and arrhythmogenesis. *Physiol Rev* 87: 457–506, 2007.
62. Terrenoire C, Clancy CE, Cormier JW, Sampson KJ, Kass RS. Autonomic control of cardiac action potentials: role of potassium channel kinetics in response to sympathetic stimulation. *Circ Res* 96: e25–e34, 2005.
63. Tsien RW, Kass RS, Weingart R. Cellular and subcellular mechanisms of cardiac pacemaker oscillations. *J Exp Biol* 81: 205–215, 1979.
64. Varghese A, Winslow RL. Dynamics of abnormal pacemaking activity in cardiac Purkinje fibers. *J Theor Biol* 168: 407–420, 1994.
65. Vinogradova TM, Bogdanov KY, Lakatta EG.  $\beta$ -Adrenergic stimulation modulates ryanodine receptor  $Ca^{2+}$  release during diastolic depolarization to accelerate pacemaker activity in rabbit sinoatrial nodal cells. *Circ Res* 90: 73–79, 2002.
66. Vinogradova TM, Brochet DX, Sirenko SG, Lyashkov AE, Maltsev VA, Yang D, Cheng H, Lakatta EG. Sarcoplasmic reticulum (SR)  $Ca^{2+}$  refilling kinetics controls the period of local subsarcolemmal  $Ca^{2+}$  releases (LCR) and the spontaneous beating rate of sinoatrial node cells (SANC) (Abstract). *Biophys J Suppl*: 31a, 2007.
67. Vinogradova TM, Lyashkov AE, Zhu W, Ruknudin AM, Sirenko S, Yang D, Deo S, Barlow M, Johnson S, Caffrey JL, Zhou YY, Xiao RP, Cheng H, Stern MD, Maltsev VA, Lakatta EG. High basal protein kinase A-dependent phosphorylation drives rhythmic internal  $Ca^{2+}$  store oscillations and spontaneous beating of cardiac pacemaker cells. *Circ Res* 98: 505–514, 2006.
68. Vinogradova TM, Sirenko S, Lyashkov AE, Younes A, Li Y, Zhu W, Yang D, Spurgeon HA, Lakatta EG. Constitutive phosphodiesterase activity restricts spontaneous beating rate of cardiac pacemaker cells by suppressing local  $Ca^{2+}$  releases. *Circ Res* 102: 761–769, 2008.
69. Vinogradova TM, Zhou YY, Bogdanov KY, Yang D, Kuschel M, Cheng H, Xiao RP. Sinoatrial node pacemaker activity requires  $Ca^{2+}$ /calmodulin-dependent protein kinase II activation. *Circ Res* 87: 760–767, 2000.
70. Vinogradova TM, Zhou YY, Maltsev V, Lyashkov A, Stern M, Lakatta EG. Rhythmic ryanodine receptor  $Ca^{2+}$  releases during diastolic depolarization of sinoatrial pacemaker cells do not require membrane depolarization. *Circ Res* 94: 802–809, 2004.
71. Wilders R. Computer modelling of the sinoatrial node. *Med Biol Eng Comput* 45: 189–207, 2007.
72. Zaza A, Robinson RB, DiFrancesco D. Basal responses of the L-type  $Ca^{2+}$  and hyperpolarization-activated currents to autonomic agonists in the rabbit sino-atrial node. *J Physiol* 491: 347–355, 1996.
73. Zhang H, Holden AV, Kodama I, Honjo H, Lei M, Varghese T, Boyett MR. Mathematical models of action potentials in the periphery and center of the rabbit sinoatrial node. *Am J Physiol Heart Circ Physiol* 279: H397–H421, 2000.
74. Zhou Z, Lipsius SL.  $Na^+$ - $Ca^{2+}$  exchange current in latent pacemaker cells isolated from cat right atrium. *J Physiol* 466: 263–285, 1993.